Nature Communications

https://doi.org/10.1038/s41467-026-74048-2

Article in Press

Chromobox 3 assembles an epigenetic complex contributing to cystathionine γ-lyase–mediated protection against aortic aneurysm/dissection

Received: 21 August 2025

Accepted: 28 May 2026

Cite this article as: Zhao, Y., Cui, C., Gao, H. *et al.* Chromobox 3 assembles an epigenetic complex contributing to cystathionine γ-lyase–mediated protection against aortic aneurysm/dissection. *Nat Commun* (2026). https://doi.org/10.1038/s41467-026-74048-2

Ying Zhao, Changting Cui, Huimin Gao, Yan Yao, Yaping Niu, Ling Cheng, Xiaodie Shao, Haizeng Zhang, Yuan Wang, Yuanzhen Lin, Zengxiang Dong, He Wu, Zhenzhen Chen, Liming Yang & Bin Geng

Chromobox 3 Assembles an Epigenetic Complex Contributing to Cystathionine γ-lyase–mediated Protection Against Aortic Aneurysm/dissection

Ying Zhao[1,2#], Changting Cui[3#], Huimin Gao[2#], Yan Yao[4#], Yaping Niu[5], Ling Cheng[2,6], Xiaodie Shao[2], Haizeng Zhang[4], Yuan Wang[2], Yuanzhen Lin[2,6], Zengxiang Dong[1], He Wu[1], Zhenzhen Chen[4*], Liming Yang[1*], Bin Geng[2*]

1. Department of Pathophysiology, Harbin Medical University; NHC Key Laboratory of Cell Transplantation, Department of Pathology, First Affiliated Hospital of Harbin Medical University; Key Laboratory of Myocardial Ischemia, Ministry of Education, Harbin Medical University, Harbin, Heilongjiang Province, China.
2. State Key Laboratory of Cardiovascular Disease, Fuwai Hospital, Chinese Academy of Medical Sciences and Peking Union Medical College, National Center for Cardiovascular Diseases, Beijing, China.
3. Department of Emergency Medicine, Beijing Key Laboratory of Cardiopulmonary Cerebral Resuscitation, Beijing Chaoyang Hospital, Capital Medical University, Beijing, China.
4. Department of Cardiology, Beijing Institute of Heart Lung and Blood Vessel Diseases, Beijing Anzhen Hospital, Capital Medical University
5. Department of Clinical Laboratory Diagnostics, Beijing Friendship Hospital, Capital Medical University, Beijing, China
6. Department of Cardiology, The First Affiliated Hospital of Wenzhou Medical University, Wenzhou, China

# These authors contributed equally to this work.

*To whom correspondence should be addressed:
Bin Geng: State Key Laboratory of Cardiovascular Disease, Fuwai Hospital, Chinese Academy of Medical Sciences and Peking Union Medical College; No. 167, North Lishi Road, Western District, Beijing, China. TEL: +86-010-60866432; E-mail: bingeng@hsc.pku.edu.cn

Liming Yang: Department of Pathophysiology, Harbin Medical University, Harbin, Heilongjiang Province, China. E-mail: limingyang@ems.hrbmu.edu.cn

Zhenzhen Chen: Beijing Institute of Heart Lung and Blood Vessel Diseases, Beijing Anzhen Hospital, Capital Medical University. Beijing, China. E-mail: chenzhenzhen@bjmu.edu.cn

Abstract

Hydrogen sulfide (H_2S), generated by cystathionine γ-lyase (CSE), protects against aortic aneurysm and dissection (AAD), yet its role in extracellular matrix (ECM) regulation remains unclear. Here, we demonstrate that CSE expression is markedly attenuated in vascular smooth muscle cells (VSMCs) from human AAD specimens and AngII-induced male murine models. VSMC-specific *Cse* deletion exacerbated AAD formation. Mechanistically, *Cse* deficiency downregulated CBX3, thereby relieving transcriptional repression of *Adamts4*. *Cbx3* overexpression rescued the aggravated AAD phenotype in *Cse*-deficient male mice. We further identified a CBX3-centered epigenetic complex (SUV39H1, KDM2A, HDAC1, RING1) that coordinates H3K9/4 methylation and acetylation to regulate ECM remodeling, apoptosis and inflammation-related genes. Notably, CSE/H_2S induced CBX3 sulfhydration at C69, C160, and C177, enhancing protein stability by reducing ubiquitin-mediated degradation; Therapeutically, AAV-mediated *Cse* or *Cbx3* delivery via an extravascular carrier attenuated AAD incidence and progression in male mice. Collectively, these findings define a VSMCs CSE/H_2S-CBX3 epigenetic axis that constrains AAD through regulation of the ADAMTS4-versican pathway.

Introduction

Aortic aneurysm/dissection (AAD) is a chronic aortic disorder characterized by progressive weakening and dilation of the vessel wall, frequently culminating in fatal rupture and accounting for an estimated 150,000 – 200,000 deaths annually worldwide[1, 2]. Hallmark pathological features include vascular smooth muscle cells (VSMCs) loss, extracellular matrix (ECM) degradation (particularly elastin and collagen), proteoglycan accumulation, and localized inflammation[3, 4]. VSMCs are central to maintaining aortic integrity through ECM synthesis, regulation of cell death, and modulation of inflammatory responses[3].

The aortic ECM is a dynamic network composed of fibrous proteins (collagen, elastin, fibrillins) and proteoglycans such as versican and aggrecan [4, 5]. Pathological ECM remodeling in AAD is driven by proteases, notably matrix metalloproteinases (MMPs), which degrade structural proteins, and ADAMTS (a disintegrin and metalloproteinase with thrombospondin motifs) proteoglycanases[6]. Versican, a large chondroitin sulfate proteoglycan predominantly expressed in VSMCs[7], plays a critical role in vascular homeostasis [8]. Versican accumulation is consistently observed in human and experimental AAD [9, 10]. Within the ADAMTS family, six members (ADAMTS1, 4, 5, 9, 15, 20) possess proteoglycanase activity[11]. ADAMTS5 exhibits the highest activity against versican, followed by ADAMTS4 and ADAMTS1[12, 13]. Notably, ADAMTS4—upregulated in both clinical and experimental AAD—cleaves versican at the Glu441-Ala442 site[14, 15], whereas ADAMTS5 is paradoxically downregulated [16]. Genetic studies confirm this functional divergence: *Adamts4* deficiency is protective against aneurysm, while loss of *Adamts1* or *Adamts5* accelerates disease[11, 17, 18]. Together, these findings underscore the importance of versicanolysis in ECM remodeling and AAD pathogenesis.

Hydrogen sulfide (H_2S), an endogenous gasotransmitter synthesized mainly by cystathionine γ-lyase (CSE), exerts vasoprotective effects via protein sulfhydration[19]. Clinical and experimental studies consistently report attenuated CSE expression and H_2S bioavailability in AAD[20, 21]. Endothelial-specific *Cse* deficiency exacerbates dissection through enhanced endoplasmic reticulum stress, a process reversed by H_2S-mediated sulfhydration of protein disulfide isomerase[21]. H_2S also inactivates MMP-2 and MMP-9 by sulfhydrating their cysteine-switch motifs[22]. While VSMCs produce MMPs, major sources of MMP-2 and MMP-9 in dissection are fibroblasts/leukocytes and macrophages, respectively[23]. Importantly,

VSMCs are the predominant producers of vascular H_2S[24]. Thus, although H_2S-mediated MMP inactivation may partly account for CSE/H_2S vasoprotection, the broader regulatory mechanisms, particularly concerning ADAMTS proteases and proteoglycan turnover, remain poorly defined.

Here, we show that VSMCs-specific *Cse* deletion aggravates AAD through epigenetic dysregulation of the ADAMTS4–versican axis. Mechanistically, *Cse* deficiency suppresses chromobox 3 (CBX3), disrupting histone H3K4/H3K9 methylation and acetylation, thereby derepressing *Adamts4* transcription. We further identify CBX3 as a scaffold for a previously unrecognized histone-modifying complex integrating methylation and acetylation pathways. Finally, local delivery of *Cse* or *Cbx3* via an absorbable extravascular carrier mitigates AAD progression, highlighting a promising translational strategy.

Results

Down-regulated VSMCs CSE expression in AAD

To examine the alterations of CSE expression in VSMCs within AAD, we performed immunofluorescence staining. Compared with healthy aortic tissues, CSE staining (green) in α-SMA–positive VSMCs (magenta) was markedly attenuated in AAD patients (Figure 1A). This observation is consistent with prior reports demonstrating decreased CSE expression in diseased aortic tissues, further supported by Western blot analyses[20, 21]. In the aorta of *Apoe*$^{-/-}$ mice, CSE expression was detectable in both endothelial cells and VSMCs, but significantly decreased in VSMCs within the AngII-induced AAD model (Figure 1B, Supplementary Figure 1). In vitro, AngII treatment notably suppressed both CSE mRNA and protein expression in human and mouse aortic smooth muscle cells (Figure 1C–F). Collectively, evidence from human samples, animal models, and cultured cells demonstrates that VSMCs-derived CSE expression is downregulated during AAD development.

VSMCs-Specific Deletion of *Cse* Promotes AAD Progression

To determine the functional role of CSE in AAD pathogenesis, we assessed phenotypic changes in two AngII-induced AAD mouse models. In the first model, AAD was established by overexpressing *Pcsk9* in the liver using AAV8-D377Y-m*Pcsk9* combined with a Paigen diet to induce hypercholesterolemia, followed by AngII infusion for four weeks. VSMCs-specific *Cse* deletion (validated in Supplementary Figure 2A, B) significantly increased AAD incidence (95.4% vs. 48%; Figure 2A), mortality (22% vs. 7%; Figure 2B), abdominal aortic diameter (1.96 mm vs. 1.42 mm; Figure 2C), and elastin degradation (Figure 2D) compared with controls.

To further confirm these results, we employed a second AAD model combining BAPN administration with AngII infusion. Consistent with findings from the AAV8-*Pcsk9* + AngII model, *Cse* deletion in VSMCs markedly elevated AAD incidence (95.6% vs. 34.4%; Figure 2E), mortality (60% vs. 16%; Figure 2F), aortic diameter (1.28 mm vs. 0.92 mm; Figure 2G), and elastin degradation (Figure 2H). Moreover, *Cse*-deficient VSMCs displayed enhanced apoptosis (Supplementary Figure 2C) and increased expression of MMP2 and MMP9 (Supplementary Figure 2D). These results strongly indicate that *Cse* deficiency in VSMCs accelerates AAD initiation and progression.

Cse Deficiency in VSMCs Induces ADAMTS4 Accumulation and Versican Degradation

ECM remodeling is a hallmark of AAD pathogenesis, driven by MMP-mediated degradation of collagen and elastin and ADAMTS-mediated degradation of proteoglycans. To elucidate the role of CSE in ECM regulation, we performed RNA sequencing of AngII-stimulated VSMCs. Transcriptomic analysis (GEO: GSE290627) revealed significant alterations in MMP and ADAMTS family members: *Mmp9*, *Mmp10*, *Mmp13*, *Adamts3*, and *Adamts4* were upregulated, whereas *Adam9* and *Adam10* were downregulated (Figure 3A, Supplementary Figure 3A). qRT-PCR validated these results, except for *Adam10* (Figure 3B, Supplementary Figure 3B), in *Cse*-deficient VSMCs following AngII exposure.

Protein analysis confirmed that *Cse* knockout augmented ADAMTS4 expression and enhanced versican degradation in VSMCs upon AngII (1 μM) stimulation for 24 hours (Figure 3C). Conversely, *Cse* overexpression suppressed ADAMTS4 expression and attenuated versican degradation (Figure 3D). Pathological staining further demonstrated elevated ADAMTS4 levels in α-SMA–positive aortic VSMCs and increased accumulation of the versican cleavage fragment V1 in Cse^{SMCKO} compared with Cse^{LOXP} mice across both AAD models (Figure 3E).

Importantly, increased ADAMTS4 expression was also detected in VSMCs from human AAD tissues (Figure 3F) and in the AngII-induced $Apoe^{-/-}$ mouse model (Figure 3G), coinciding with pronounced versican degradation. These findings, consistent with previous studies[14, 15], underscore a critical role of the ADAMTS4–versican axis in mediating CSE-regulated ECM remodeling during AAD pathogenesis.

CBX3 Negatively Regulates ADAMTS4 Expression

Polycomb repressive complexes (PRC1 and PRC2) are central epigenetic regulators that silence gene transcription through histone modification. To identify PRC components involved in ADAMTS4 regulation, we analyzed downregulated genes from RNA-seq datasets and validated candidates by qRT-PCR. Both *Cbx3* and *Ezh2* expression were significantly attenuated following *Cse* deletion (Figure 4A; Supplementary Figure 4A). To determine their functional roles, we performed siRNA-mediated knockdown studies in VSMCs. Silencing *Ezh2* decreased *Adamts4* mRNA expression, whereas *Cbx3* knockdown markedly increased *Adamts4* transcription (Supplementary Figure 4B, C), indicating that CBX3 acts as a transcriptional repressor of ADAMTS4. Consistently, Western blot analysis showed that

Cbx3 knockdown increased ADAMTS4 protein levels and enhanced versican cleavage, whereas *Ezh2* silencing attenuated ADAMTS4 expression and versican cleavage (Supplementary Figure 4D). Although both CBX3 and EZH2 independently modulated ADAMTS4 expression, simultaneous knockdown of *Cbx3* and *Ezh2* produced a phenotype comparable to *Cbx3* silencing alone. These findings suggest that CBX3 plays a dominant role in regulating *Adamts4* transcription.

Western blot analysis confirmed attenuated CBX3 protein levels after *Cse* deletion (Supplementary Figure 5A) with AngII or ox-LDL stimulation (Figure 4B). Immunofluorescence demonstrated that CBX3 predominantly localized in the nucleus but was diminished in *Cse*-deficient VSMCs (Figure 4C), whereas *Cse* overexpression enhanced CBX3 expression (Figure 4D). In vivo, CBX3 expression was significantly attenuated in VSMCs of Cse^{SMCKO} mice compared with controls in two AAD models (Figure 4E). Similar downregulation was observed in VSMCs from AAD patients and $Apoe^{-/-}$ mice (Figure 4F).

To investigate its functional role, primary VSMCs from *Cse*-knockout mice were examined. Knockdown of *Cbx3* further increased ADAMTS4 expression and versican cleavage (Figure 4G, Supplementary Figure 5B), whereas *Cbx3* overexpression suppressed both (Figure 4H). In contrast, overexpression of *Cse* in *Cbx3*-deficient VSMCs did not alter ADAMTS4 levels or versican cleavage (Supplementary Figure 5C). Together, these results identify CBX3 as a nuclear effector that mediates the regulatory link between endogenous CSE/H_2S signaling and ADAMTS4 expression.

Cbx3 Overexpression Attenuates *Cse* Deficiency–Induced AAD

To determine whether restoring *Cbx3* could mitigate AAD progression driven by *Cse* deficiency, we developed a localized gene delivery system. A collagen-based absorbable extravascular stent-like carrier was implanted around the superior renal artery, adsorbing AAV9-sm22α-*Cbx3* to achieve targeted *Cbx3* overexpression; AAV9-sm22α-*GFP* served as control (Supplementary Figure 6). One week later, mice were subjected to BAPN + AngII to induce AAD.

Among survivors (14/group), *Cbx3* overexpression significantly attenuated AAD incidence (4/14 vs. 12/14; Figure 5A, B), aortic dilation (Figure 5C), elastin degradation, and collagen deposition (Figure 5D). Moreover, pathological hallmarks of AAD progression—including versican cleavage (Figure 5E), ADAMTS4 accumulation (Figure 5F), VSMCs apoptosis (TUNEL staining, Figure 5G), macrophage

infiltration (CD68 positive cells), and elevated MMP2/9 (Figure 5H)—were all attenuated by *Cbx3* overexpression. Collectively, these data demonstrate that *Cbx3* restoration rescues the exacerbated AAD phenotype in *Cse*-deficient mice, primarily via the CBX3–ADAMTS4–versican signaling axis.

Histone Modifications Mediate CBX3's Response to *Cse* Deletion

CBX3 is tightly linked to histone modifications across various cell types[25, 26]. To determine whether epigenetic alterations contribute to CBX3-mediated regulation in AAD, we examined global histone marks following CSE manipulation. *Cse* deletion alone, as well as AngII or ox-LDL treatment, significantly decreased H3K9me3, H3K9ac, H3K4me3, and H3K4ac levels, whereas H3K27me3 remained unchanged (Figure 6A; Supplementary Figure 7A). In contrast, *Cse* overexpression enhanced H3K4 and H3K9 methylation and acetylation (Figure 6B). Displayed attenuated H3K9me3/ac and H3K4me3/ac levels in the aorta in two independent AngII-induced AAD models (Figure 6C, 6D). Comparable reductions were observed in human AAD tissues (Supplementary Figure 8A) and in *Apoe*$^{-/-}$ mice (Supplementary Figure 8B), suggesting that impaired H3K4/9 methylation/acetylation represents a common epigenetic mechanism in AAD. To further define the role of CBX3, we manipulated its expression in VSMCs. *Cbx3* silencing in WT VSMCs attenuated H3K4/9 methylation and acetylation (Supplementary Figure 7B), and knockdown in *Cse*-deficient VSMCs further exacerbated the loss of these marks (Figure 6E). Conversely, *Cbx3* overexpression restored H3K4/9 methylation and acetylation under AngII stimulation (Figure 6F). Together, these findings establish CBX3 as a key mediator of CSE-dependent histone remodeling in AAD.

CSE–CBX3–Histone Modification Axis in AAD

To elucidate the underlying epigenetic mechanisms, we integrated ChIP-seq and RNA-seq analyses in VSMCs. *Cse* deletion led to a marked increase in H3K9me3 enrichment around transcription start sites (TSS ± 3 kb; Figure 7A), affecting 355 genes, of which 92 were upregulated and 263 were downregulated. Gene Ontology and KEGG pathway analyses of these targets revealed significant enrichment in ECM regulation, apoptosis, VSMCs function, and inflammatory signaling (Figure 7A and Supplementary Figure 9A-C). In contrast, *Cse* deficiency was associated with a global reduction in

activating histone marks, including H3K9ac and H3K4me3 (Figure 7B, C). Locus-specific inspection using IGV demonstrated concordant decreases in histone modification signals at key genes involved in ECM remodeling (*Adamts4, Mmp9, Col1a2*), inflammation (*Nlrp3*), and apoptosis (*Bcl2*) (Figure 7D, E). These findings were further validated by ChIP-qPCR, which confirmed significantly attenuated enrichment of H3K9me3/ac and H3K4me3/ac at the promoters of *Adamts4*, *Mmp9*, *Col1a2*, *Nlrp3*, and *Bcl2* in *Cse*-deficient VSMCs compared with WT controls (Supplementary Figure 10). Collectively, these data indicate that the CSE-CBX3 axis modulates histone H3K4 and H3K9 modifications to coordinately regulate ECM remodeling, apoptosis, and inflammatory pathways, thereby contributing to the molecular pathogenesis of AAD.

CBX3 as a Component of an Epigenetic Regulatory Complex

CBX3, a heterochromatin protein 1 (HP1)–interacting factor, is known to function as an H3K9me3 methyl-reader; however, its role in modulating other histone marks such as H3K9ac, H3K4me3, and H3K4ac remains unclear. To identify CBX3-binding partners, we performed immunoprecipitation (IP) followed by proteomic analysis. SDS-PAGE with silver staining (Supplementary Figure 11A) revealed distinct protein bands, which were analyzed by mass spectrometry, identifying 405 potential CBX3 interactors (Supplementary Data 5). GO and KEGG analyses showed significant enrichment in histone binding and modification pathways (Supplementary Figure 11B).

For validation, plasmids encoding Flag-tagged *CBX3*, HA-tagged *KDM2A*, Myc-tagged *HDAC1*, His-tagged *RING1*, and Strep-tagged *SUV39H1* were co-transfected in random pairs into HEK293T cells. Co-immunoprecipitation confirmed CBX3 interactions with RING1, SUV39H1, KDM2A, and HDAC1 (Figure 8A). These interactions were further validated in primary mouse aortic VSMCs (Figure 8B). Notably, *Cse* deletion disrupted CBX3 interactions with KDM2A and SUV39H1, while strengthening its association with HDAC1 (Figure 8C). Collectively, these findings indicate that CBX3 forms a dynamic epigenetic regulatory complex with SUV39H1, KDM2A, HDAC1, and RING1, responsive to changes in the CSE/H_2S system, thereby contributing to AAD pathogenesis.

CBX3 Sulfhydration Attenuates AngII-Induced Ubiquitin-Mediated Degradation

To determine why *Cse* deficiency attenuated CBX3 protein levels, we examined CBX3 sulfhydration, a post-translational modification mediated by H_2S. Using a biotin-switch assay, we detected CBX3 sulfhydration in vitro in liver (Figure 9A) and aortic (Figure 9B) homogenates, as well as in vivo in VSMCs (Figure 9C). *Cse* deletion markedly attenuated CBX3 sulfhydration compared with WT cells (Figure 9D). AngII similarly suppressed CBX3 sulfhydration, whereas the CSE agonist norswertianolin (NW) restored it (Figure 9E, F), indicating that CBX3 sulfhydration depends on the CSE/H_2S axis and is inhibited by AngII.

Human *CBX3* contains three conserved cysteine residues (C69, C160, C177). Single and triple cysteine-to-serine mutants demonstrated that all three sites contribute to NaHS-induced sulfhydration. Mutation of these residues abolished CBX3 sulfhydration-mediated regulation of H3K9me3 and H3K9ac (Figure 9G, H), supporting their functional relevance.

To assess protein stability, VSMCs were pretreated with cycloheximide to inhibit protein synthesis. AngII markedly accelerated CBX3 degradation (Figure 9I), whereas the H_2S donor NaHS and the CSE activator NW attenuated this effect (Figure 9J). Similar AngII-induced CBX3 degradation was observed in HEK-293T cells expressing WT *CBX3* (Supplementary Figure 12A). Importantly, mutation of the sulfhydration sites abolished the protective effect of H_2S on CBX3 stability (Figure 9K and L). Moreover, the proteasome inhibitor MG-132 blocked AngII-induced CBX3 degradation (Supplementary Figure 12B). NaHS attenuated CBX3 ubiquitination, whereas cysteine mutation reversed this inhibitory effect (Supplementary Figure 12C), indicating that CBX3 sulfhydration prevents ubiquitin-mediated proteasomal degradation. Together, these findings demonstrate that CSE-derived H_2S stabilizes CBX3 via cysteine sulfhydration, thereby preventing AngII-induced ubiquitin–proteasome degradation.

Local Overexpression of *Cse* or *Cbx3* Attenuates AAD Development

To assess the therapeutic potential of CSE or CBX3 restoration, we implanted a collagen sponge–based absorbable extravascular stent around the abdominal aorta (between the diaphragm and renal artery) loaded with AAV9-sm22α-*Cse* or AAV9-sm22α-*Cbx3*. *Apoe*$^{-/-}$ mice underwent AngII infusion one week after implantation. Four weeks later, both *Cse* and *Cbx3* overexpression markedly attenuated AAD incidence (Figure 10A), aortic diameter (Figure 10B), elastin degradation, and collagen deposition (Figure

10C). Additionally, apoptotic cell counts (TUNEL, Supplementary Figure 13B), macrophage infiltration (CD68 staining), and MMP2/MMP9 expression (Supplementary Figure 13C) were significantly decreased in both treatment groups.

Consistent with these phenotypic changes, *Cse* or *Cbx3* overexpression also attenuated ADAMTS4 accumulation and versican cleavage in the aortic media (Figure 10D, E). Interestingly, *Cse* overexpression partially restored CBX3 expression to levels comparable with direct *Cbx3* overexpression (Figure 10D), whereas *Cbx3* overexpression did not affect CSE expression (Supplementary Figure 13A), confirming CBX3 as a downstream effector of CSE in vivo.

Together, these findings demonstrate that targeted, VSMCs-specific overexpression of *Cse* or *Cbx3* via AAV-based delivery using an absorbable extravascular carrier effectively suppresses AAD progression, highlighting a therapeutic strategy based on the CSE–CBX3–ADAMTS4 axis.

Discussion

VSMCs are the main producers of CSE and H_2S in arterial tissues, regulating VSMCs functions such as contraction, proliferation, migration, apoptosis and senescence[19, 24, 27]. H_2S influences key proteins via sulfhydration, inhibiting MMP2/MMP9 activity[22] and reducing endoplasmic reticulum stress[21, 28], thereby modulating AAD progression. However, direct evidence linking VSMCs-specific CSE/H_2S signaling to AAD remains limited. In this study, we observed attenuated CSE expression in VSMCs from AAD patients and murine models. Using a conditional knockout mouse model, we found that *Cse* deletion in VSMCs worsened AAD in two AngII-induced models. Mechanistically, *Cse* loss disrupted the CBX3 epigenetic complex, altering histone modifications and promoting *Adamts4* transcription, and dysregulation of *Mmp9*, *Col1a2*, *Nlrp3*, and *Bcl2*. These changes exacerbated versican cleavage, collagen/elastin degradation, inflammation, and apoptosis, accelerating AAD development (Supplementary Figure 14).

Previous studies have shown attenuated aortic CSE expression in AAA and aortic dissection patients, as well as in the aortic endothelium of AngII-induced *Apoe*$^{-/-}$ mice[20, 21]. Our study further confirms CSE downregulation in VSMCs of AAD patients and an AngII-induced mouse model using immunofluorescence staining. Risk factors for AAD, such as aging (including cell senescence and senility), male gender, hypertension, hypercholesterolemia, and diabetes (high glucose). Notably, several studies have reported that high glucose levels and hypercholesterolemia are linked to decreased VSMCs CSE expression[17, 23, 27]. AngII, a key AAD inducer, directly suppresses CSE in VSMCs and endothelial cells [21, 27, 30], via transcriptional repression by the ZEB2-HDAC1-NuRD complex and post-translational including HDAC6-mediated acetylation at K73 and ubiquitination at K48, leading to CSE degradation[21, 30, 31, 32]. These findings highlight how risk factors accelerate CSE reduction in aortic VSMCs, contributing to AAD pathogenesis and progression.

The histopathological hallmark of ECM remodeling in AAD is characterized by the degradation and disorganization of elastic and collagen fibers, along with proteoglycan accumulation [6]. Among the major large proteoglycans, versican and aggrecan play crucial roles in maintaining the reversible compressive structure of the aortic wall, regulating VSMCs homeostasis, and are notably upregulated in thoracic aortic aneurysm and dissection (TAAD) [9, 33]. The ADAMTS family members (ADAMTS1, ADAMTS4, and

ADAMTS5) exhibit proteolytic activity toward aggrecan and versican[7], with their protein expression significantly elevated in TAAD patients[6]. Genetic studies in mice reveal divergent roles for these proteases: *Adamts1* heterozygosity exacerbates high-fat diet plus AngII-induced aortic events but attenuates BAPN plus AngII-induced pathology[17, 34]. Deletion of the *Adamts5* catalytic domain enhances AngII-induced ascending aortic dilation[18]. Global *Adamts4* knockout mitigates AngII-induced AAD formation, versican degradation, elastic fiber destruction, macrophage infiltration, and VSMCs apoptosis[15]. In our current study, smooth muscle cell-specific *Cse* knockout mice exhibited exacerbated AngII-induced AAD incidence and progression, correlating with ADAMTS4 accumulation and heightened versican degradation. Consistent with prior findings on ADAMTS4-versican dysregulation, we observed concomitant increases in elastic fiber degradation, macrophage infiltration, and VSMCs apoptosis, mirroring the phenotypic consequences of *Adamts4* deletion[15]. RNA-seq analysis further confirmed that *Adamts1* and *Adamts5* expression remained unchanged in *Cse*-deficient VSMCs compared to wild-type controls. These findings collectively implicate ADAMTS4-versican axis dysregulation as a key mechanism underlying ECM remodeling, inflammatory responses, and cell death in AAD pathogenesis, mediated by VSMCs CSE/H_2S signaling. Importantly, human AAD samples corroborated these results, demonstrating elevated ADAMTS4 expression and versican degradation—phenotypes also observed in TAAD[14, 15], and traditional murine AAD models. Therefore, ADAMTS4 upregulation represents a conserved pathophysiological mechanism in AAD, suggesting that targeted inhibition of this protease may hold therapeutic potential for preventing or treating AAD.

Adamts4 transcription is bidirectionally regulated by SP1/AP-2α (activators) and nuclear factor I (NFI)/histone H4 deacetylation (repressors) [35, 36]. While CSE/H_2S inhibits SP1 via sulfhydration-mediated suppression of Jumonji domain-containing protein 3 and MMP2[22, 37], its effects on AP-2α/NFI/H4 remain unknown. Here, we identified CBX3 as a negative regulator of *Adamts4* transcription. CBX3 levels were significantly attenuated in both *Cse*-deficient VSMCs/aortic tissues and human/murine AAA specimens. Functional studies demonstrated that localized *Cbx3* overexpression in *Cse*-deficient VSMCs attenuated AAD progression, concomitant with decreased ADAMTS4 expression and versican cleavage. These

findings establish CBX3 as a previously unidentified transcriptional repressor in the ADAMTS4 regulatory network, providing mechanistic insights into AAD pathogenesis.

The CBX family proteins are canonical components of PRC1, which is a well-characterized transcriptional repressor primarily mediating gene silencing through H2AK119 ubiquitination[37]. CBX3 exhibits dual functions as both a PRC1 component and an H3K9me3 reader through its interaction with HP1 complexes and SUV39H1/2 methyltransferases[38]. It regulates diverse processes including VSMCs proliferation and migration (via Notch3 signaling)[39], interfering artery development (via smooth muscle cells differentiation) [40], and H4K20me3-dependent cardiac growth[25]. Recent studies show CBX3 recruits EP300 to promote histone lactylation[41]. In this study, we identify CBX3 as a specific regulator of H3K9me3/ac and H3K4me3/ac, but not H3K27me3. Proteomic and Co-IP analyses reveal CBX3 forms an epigenetic complex with SUV39H1, KDM2A, HDAC1, and RING1. These interactions suggest the formation of a histone-modifying complex centered around CBX3. ChIP-seq also demonstrates CSE-induced CBX3 downregulation alters these marks at loci involved in ECM remodeling, apoptosis, and inflammation - key pathways in AAD pathogenesis. We propose CBX3 serves as a scaffold coordinating methylase/demethylase (SUV39H1/KDM2A), acetyltransferase/deacetylase (EP300/HDAC1), and ubiquitin ligase (RING1) activities, forming a transcriptional repressor module that drives AAD development through integrated histone modification control.

Post-translational modifications critically regulate CBX3 stability and function. Previous studies have shown that citrullination of CBX3 at R38 and R39 enhances its binding to H3K9me3 and facilitates mESC differentiation[42], whereas LINC00998 interaction stabilizes CBX3 by preventing its ubiquitin-mediated degradation[43]. In the present study, we identify sulfhydration as a previously unrecognized modification of CBX3. Specifically, CBX3 undergoes sulfhydration at C69, C160, and C177, which inhibits its ubiquitination and proteasomal degradation. Mechanistically, AngII suppresses the CSE/H_2S axis, leading to attenuated CBX3 sulfhydration and accelerated CBX3 degradation. These findings uncover a post-translational regulatory mechanism whereby CSE/H_2S maintains CBX3 stability through sulfhydration, thereby influencing downstream epigenetic regulation.

AAD progression involves complex pathophysiological processes, including inflammation, oxidative stress, and apoptosis. Protein S-sulfhydration is a key post-translational modification mediating

the biological effects of H_2S. S-sulfhydration of MMPs suppresses their enzymatic activity, thereby limiting collagen and elastin degradation[22]. In this study, CBX3 sulfhydration attenuates ADAMTS4–versican signaling, contributing to ECM stabilization and highlighting the role of sulfhydration in ECM remodeling. Additionally, PDI sulfhydration enhances its activity and alleviates ER stress in endothelial cells[28]. Endothelial-specific *Cse* deletion promotes AAD by exacerbating inflammation[21]. In addition, VSMCs-specific *Cse* deficiency also reduces PDI sulfhydration (data not shown), which may enhance ER stress–induced apoptosis in VSMCs, leading to VSMCs loss and further progression of AAD. Notably, *Cse* overexpression restores sulfhydration of MMPs, CBX3, and PDI, reducing ECM degradation, inflammation, and apoptosis, thereby exerting protective effects against AAD.

Open surgery (OS) and endovascular aneurysm repair (EVAR) are the primary therapeutic strategies for AAD. Short-term outcomes favor EVAR due to its advantages, including shorter operation times, attenuated intraoperative blood loss, decreased need for blood transfusions, and lower rates of postoperative mechanical ventilation[44, 45, 46]. However, long-term mortality rates do not significantly differ between OS and EVAR, likely because EVAR requires more frequent secondary interventions—often due to graft-related complications such as endoleaks[44]. To address these limitations, we developed an "extravascular stent-like carrier" composed of a collagen sponge, which offers several key benefits: (1) prevention of aneurysm rupture, (2) biodegradability, and (3) the capacity to deliver therapeutic agents (e.g., viruses or drugs) for localized treatment. In our approach, the carrier was implanted around the abdominal aorta between the diaphragm and renal artery—the most susceptible site for aneurysm formation in an AngII-induced AAD mouse model. This placement effectively attenuated aneurysm rupture. Additionally, we loaded the carrier with AAV9 vectors to overexpress *Cse* or *Cbx3* in VSMCs, which significantly attenuated AngII-induced AAD incidence and progression. Collectively, our findings suggest that implantation of an extravascular stent combined with localized gene therapy may represent a promising alternative therapeutic strategy for AAD.

Limitations of the current study include the following: 1) Lack of VSMCs-specific *Cbx3* inducible knockout mice. These mice would have been valuable to confirm whether the protective effects of H_2S donors on AAD are mediated through CBX3. 2) The study did not explore whether CSE/H_2S signaling regulates CBX3 transcription/translation, and its regulatory model of the epigenetic complex. 3) The

causal hierarchy between CSE-mediated cysteine metabolism, epigenomic remodeling, and CBX3 function remains incompletely resolved. Specifically, we cannot exclude the possibility that *Cse* deficiency primarily alters the epigenome, thereby secondarily affecting CBX3 expression and downstream signaling, a mechanism that would require integrative approaches such as ATAC-seq to clarify. 4) Only the AngII-induced AAD model was used; other established models, such as elastase-induced or $CaCl_2$-induced aortic aneurysm, were not examined. 5) Key translational questions of extravascular stent challenges in large animals remain unresolved, including material optimization, biomechanical parameters, and therapeutic efficacy in preclinical large-animal AAD models.

In summary, our study identifies VSMCs-derived CSE/H_2S as a critical regulator of AAD development and reveals a CBX3-centered epigenetic mechanism linking H_2S signaling to vascular remodeling. We show that loss of CSE/H_2S reduces CBX3 sulfhydration, promotes its ubiquitin-mediated degradation, and disrupts a CBX3-containing epigenetic complex, leading to alterations in H3K9 and H3K4 methylation and acetylation. These changes drive pathogenic gene expression programs controlling ECM remodeling, apoptosis, and inflammation, including upregulation of ADAMTS4 and versican degradation. As an initial translational exploration, we evaluated a combined approach of extravascular stenting with localized AAV-mediated delivery of *Cse* or *Cbx3*, which showed potential to modulate key molecular pathways and support the aortic wall. While preliminary, these findings suggest a possible proof-of-concept for targeted intervention in AAD.

Methods

All experimental procedures in this study were performed in accordance with the relevant ethical guidelines and regulations. The human study protocol was reviewed and approved by the Ethics Committee of the First Affiliated Hospital of Harbin Medical University (2025141). The animal study protocol was reviewed and approved by Institute of Animal Care and Use Committee of Fuwai Hospital, Chinese Academy of Medical Sciences (FW-2020-0059).

The data, research methods, and study materials utilized in this study are available from the corresponding authors on reasonable request.

Human Aortic Samples

The human aortic tissues were collected in compliance with the Decleration of Helsinki. Written informed consent was obtained from all participants or their legal representatives prior to the collection of human aortic samples. The AAD aortic samples were collected from patients who suffered aneurysmectomy and vascular transplantation. The non-AAD samples were from the Biospeciman Bank of the First Affiliated Hospital of Harbin Medical University. The baseline characteristics of the patients are presented in Supplementary Data 1. The study was approved by the Ethics Committee of the First Affiliated Hospital of Harbin Medical University (2025141).

Animal Study and AAD Models

All mice were housed in a specific pathogen-free (SPF) animal facility under controlled environmental conditions: constant temperature 22–25°C, humidity 50–60%, and a 12 h light/12 h dark cycle. Animals had free access to standard laboratory chow (XT93G, Jiangsu Xietong Pharmaceutical Bio-engineering, Nanjing, China) or a Paigen diet (D12109C, Research diets, USA). Animal experiments were approved by Institute of Animal Care and Use Committee of Fuwai Hospital, Chinese Academy of Medical Sciences (FW-2020-0059), and performed in accordance with the animal experiment guidelines.

Cse^{SMCKO} knockout mice generated by *Cse*^{LOXP} (containing loxP sites flanking exons 2 and 3) hybridzation with Tagln-Cre mice as our previous study[24]. *Apoe* knockout mice (*Apoe*$^{-/-}$) and C57BL/6J mice were purchased by Charles River Laboratories (Beijing, China).

All mouse genomic DNA was genotyped by PCR amplification with specific primers provided in Supplementary Data 2.

AngII-induced AAD model was performed as previously described[47]. Briefly, 8- to 10-week-old male *Apoe*$^{-/-}$ mice were subcutaneously implanted with minipumps (Alzet, Model 2004, Durect Corporation, CA, USA) to infuse AngII (1000ng/kg/min) (A9525, Sigma, USA) for 4 weeks while being maintained on a Paigen diet (D12109C, Research diets) to induce AAD.

The AAV8-*Pcsk9*/AngII-induced AAD model was established following established protocols[48]. Briefly, 8- to 10-week-old male mice (*Cse*^{LOXP}, *Cse*^{SMCKO}) received intravenous injection of recombinant adeno-associated virus (rAAV8-HCRApoE/hAAT-D377Y-m*Pcsk9*; 5×10^{11} vector genome copies in 150 μl sterile saline) (WZ Biosciences Inc., Jinan, China) while being maintained on a Paigen diet to induce hyperlipidemia. One week post-AAV administration, AngII (1,000 ng/kg/min) was continuously delivered via subcutaneous osmotic minipump for 4 weeks to promote AAD development.

The β-aminopropionitrile (BAPN, A3134-25g, Sigma, St Louis, MO, USA)/AngII-induced AAD model was established as previously described[49]. Briefly, 8- to 10-week-old male mice received concurrent administration of AngII (1,000 ng/kg/min) via osmotic minipump and BAPN (150 mg/kg/day) in drinking water for 4 weeks to induce aortic aneurysm formation.

At 28 days post-modeling, the maximum abdominal aortic diameters were assessed by ultrasound using the Vevo 3100 platform (Visual Sonics, Toronto, CA) and MS-250 transducer (FUJIFILM VisualSonics). Mice were anaesthetized with 2% isoflurane and placed on a 37°C heated plate. We performed a standardized imaging algorithm with longitudinal B-mode images during the systolic phase to obtain the inner aortic diameters. For all the experiments, the investigators were blinded to the group allocations during the measurements and data analysis, and the mice were tested in a randomized order.

Extravascular Stent Implantation Using a Collagen Sponge

The procedure began with a blunt dissection of the abdominal aorta between the diaphragm and the right renal artery, the intended site for AngII-induced murine AAD formation. Following dissection, an absorbable collagen sponge was implanted around the aorta to serve as an extravascular stent. To facilitate localized gene overexpression, 50μl of sterile saline containing adeno-associated virus (AAV; 5×10^{11} genome copies) was applied directly to the collagen sponge. The abdominal incision was then closed and

disinfected. Postoperatively, subcutaneous penicillin injections were administered for three days to prevent infection. After a one-week recovery period, the AngII infusion protocol for AAA induction was initiated.

A total of 28 8-week-old male *Cse*^{SMCKO} mice were randomly divided into two groups, with 14 mice in each group: 1) *Cse*^{SMCKO} mice + AAV9-sm22α-*GFP* + BAPN + AngII group (AAV9-*GFP*); 2) *Cse*^{SMCKO} mice + AAV9-sm22α-*Cbx3* + BAPN + AngII group (AAV9-*Cbx3*). The modeling period was 28 days, during which all mice were fed with a standard laboratory chow diet, and the AAA model was induced by BAPN-containing drinking water combined with subcutaneous implantation of AngII osmotic pumps. The operation procedures for virus injection, abdominal incision, and local delivery were the same as described above.

Thirty 8-week-old male *Apoe*$^{-/-}$ mice were randomly divided into three groups, with 10 mice in each group: the AAV9-sm22α-*Cse* group (AAV9-*Cse*), the AAV9-sm22α-*Cbx3* group (AAV9-*Cbx3*), and the AAV9-sm22α-*GFP* group (AAV9-*GFP*). The operation procedures for virus injection, abdominal incision, and local delivery were the same as described above.

The adeno-associated virus were packaged and provided by WZ Biosciences Inc. (Jinan, China).

Primary Culture of Vascular Smooth Muscle Cells

Primary vascular smooth muscle cells were isolated from 6–8-week-old male wild-type and *Cse* global knockout (*Cse*$^{-/-}$) mice. The cells were cultured in Dulbecco's Modified Eagle Medium (DMEM) supplemented with 20% fetal bovine serum (FBS; Gibco, 10099141C, USA) and 10% penicillin-streptomycin (Pen Strep; Gibco, 15140-122, USA). The culture medium was refreshed every two days, and cells were maintained in a humidified incubator at 37 °C with 5% CO_2 and 95% air. Primary VSMCs between passages three and eight were used for subsequent experiments.

Maintenance and Culture of Human Aortic Smooth Muscle Cells (HASMCs)

Human aortic smooth muscle cells (HASMCs) were obtained from the American Type Culture Collection (ATCC; GF3158C, USA). Cells were cultured in smooth muscle cell–specific growth medium (ScienCell Research Laboratories, 1101, USA) according to the manufacturer's instructions. The medium

was replaced every 48 hours. Cells were maintained in a humidified incubator at 37 °C under an atmosphere of 5% CO_2 and 95% air. Only cells between passages 3 and 8 were used for experiments to ensure phenotypic stability.

Protein Extraction and Western Blot Analysis

Cells were lysed in RIPA buffer (Solarbio, R0010, Beijing, China) containing protease and phosphatase inhibitor cocktails. The lysates were centrifuged at 12000× g for 10 minutes at 4°C, and the supernatant was collected for protein quantification using a bicinchoninic acid (BCA, Solarbio, PC0020, Beijing, China) assay. Protein samples (20 μg per lane) were resolved by sodium dodecyl sulfate–polyacrylamide gel electrophoresis (SDS-PAGE) and subsequently transferred onto nitrocellulose membranes (Millipore, HATF00010, USA). The membranes were blocked with 5% non-fat milk for 1 hour at room temperature, followed by overnight incubation at 4°C with primary antibodies targeting the proteins of interest. After washing with Tris-buffered saline containing Tween-20 (TBST), the membranes were incubated with horseradish peroxidase (HRP)-conjugated secondary antibodies for 1 hour at room temperature. Protein bands were visualized using a chemiluminescence detection kit following additional TBST washes. The following primary antibodies were used for Western blot analysis: anti-SUV39H1 (1:1000, D11B6, CST), anti-H3K9me3 (1:2000, ab8898, abcam), anti-H3K9ac (1:2000, ab32129, Abcam), anti-H3K4me3 (1:2000, ab8580, Abcam), anti-H3K4ac (1:2000, ab176799, Abcam), anti-H3K27me3 (1:2000, ab6002, Abcam), anti-CBX3 (1:1000, ab217999, Abcam), anti-RING1 (1:1000, ab180170, Abcam), anti-KDM2A (1:1000, ab191387, Abcam), anti-HDAC1 (1:1000, ab280198, Abcam), anti-VERSICAN (1:1000, ab19345, Abcam), anti-ADAMTS4 (1:1000, ab185722, Abcam), anti-CSE (1:1000, ab151769, Abcam), anti-GAPDH (1:10000, Af2823, Beyotime), anti- HA-HRP (1:500, H1103, LABLEAD), anti-His-HRP (1:500, H1104, LABLEAD), anti-Myc-HRP (1:500, M1102, LABLEAD), Anti-DDDDK tag (1:1000, ab205606, Abcam).

RNA preparation and RT-qPCR analysis

Total RNA was extracted from treated samples using TRIzol® reagent (Invitrogen, 15596026CN, USA) according to the manufacturer's protocol, followed by DNase I treatment to eliminate genomic DNA contamination. RNA concentration and purity were verified spectrophotometrically (A260/A280

ratio⩾1.8). First-strand complementary DNA (cDNA) was synthesized from 1μg of total RNA using a High-Capacity cDNA Reverse Transcription Kit (Thermo Scientific, K1622, USA) with random hexamer primers. Quantitative real-time PCR (qRT-PCR) was performed using SYBR Green PCR Master Mix kit (Yeasen Biotechnology, 11201ES08, Shanghai, China). No-template controls (NTCs) and no-reverse transcription controls (NRTs) were included to rule out contamination and genomic DNA amplification, respectively. Relative gene expression was calculated using the comparative $2^{-\Delta\Delta Ct}$ method, with *Gapdh* serving as the endogenous reference. Primer sequences are provided in Supplementary Data 3.

siRNA and Plasmid Transfection

The siRNA targeting mouse *Cbx3* (si*Cbx3*), *Ezh2* (si*Ezh2*) and negative control siRNA (si*Con*) were provided by Shanghai Primerna NAT Co., Ltd (Shanghai, China). The sequences used were as follows: negative control siRNA sense, 5′-UUCUCCGAACGUGUCACGU-3′ and antisense 5′-ACGUGACACGUUCGGAGAA-3′; *Cbx3* siRNA sense, 5′ CCUGAAGAAUUUGUGGUAGAA-3′ and antisense, 5′-UUCUACCACAAAUUCUUCAGG-3′. *Ezh2* siRNA sense, 5′GCUAGGCUAAUUGGGACCAAA-3′ and antisense, 5′-UUUGGUCCCAAUUAGCCUAGC-3′. All plasmids were constructed by WZ Biosciences Inc. (Jinan, China).

Vascular smooth muscle cells (VSMCs) were seeded in 6-well plates and transfected at approximately 70% confluency. Transfection was performed using 2 μg of plasmid or 200 nM siRNA mixed with Lipofectamine 3000 reagent (Thermo Fisher Scientific, L3000075, USA) according to the manufacturer's protocol. Following a 6-hour incubation period, the transfection medium was replaced with standard culture medium, and cells were cultured for an additional 48 hours before mRNA and protein expression levels were assessed.

Immunofluorescence Staining

Aortic Tissue Staining

Aortic Aneurysm/dissection (AAD) specimens were fixed in 4% paraformaldehyde (PFA, Solarbio, P1110, Beijing, China) immediately after isolation. After 24 hours of fixation, tissues were paraffin-embedded and sectioned. The sections were treated with 3% hydrogen peroxide to quench endogenous

peroxidase activity. Antigen retrieval was performed by heating the sections in citrate buffer (95 °C, 20 min), followed by cooling to room temperature.

VSMCs Staining

For cellular immunofluorescence, VSMCs were fixed in 4% PFA for 15 min at room temperature, washed three times with phosphate-buffered saline (PBS, Solarbio, P1010, Beijing, China), and permeabilized with 0.5% Triton X-100 (15 min, room temperature, Sigma, X100, USA).

Immunostaining Procedure

Both tissue sections and cells were blocked with 1% bovine serum albumin (BSA, Sigma, V900933, USA) for 1 hour, then incubated overnight at 4°C with primary antibodies. After washing, samples were incubated with fluorophore-conjugated secondary antibodies for 1 hour at room temperature. Nuclei were counterstained with 4′,6-diamidino-2-phenylindole (DAPI, Sigma, D9542, USA) for 10 min. Fluorescence images were acquired using either a fluorescence microscope or a confocal laser scanning microscope. The following primary antibodies were used: anti-CSE (1:500, ab151769, Abcam), anti-CBX3 (1:500, ab217999, Abcam), anti-α-SMA (1:500, ab7817, Abcam), anti-H3K9me3 (1:1000, ab8898, Abcam), anti-H3K9ac (1:1000, ab32129, Abcam), anti-H3K4me3 (1:1000, ab8580, Abcam), anti-H3K4ac (1:1000, ab176799, Abcam), Goat anti-Rabbit IgG H&L (Alexa Fluor® 488) (1:500, ab150077, abcam), Goat anti-mouse IgG H&L (Alexa Fluor® 594) (1:500, ab150116, abcam).

Histological and Immunohistochemical Analyses

Elastic Fiber Staining

Paraffin-embedded aortic sections were stained using an Aldehyde-Fuchsin Stain Solution Kit (Solarbio, G1594, Beijing, China) following the manufacturer's protocol. Elastic fiber morphology was subsequently examined by light microscopy.

Evaluation and Analysis of Elastin Degradation (1–4 Points):

1 point: Elastin degradation less than 25%; 2 points: Elastin degradation of 25%–50%; 3 points: Elastin degradation of 50%–75%; 4 points: Degradation rate greater than 75%.

Masson's Trichrome Staining

Aortic tissue sections were deparaffinized through xylene immersion and graded ethanol rehydration. Collagen deposition was assessed using a Masson's Trichrome Stain Kit (Sigma-Aldrich, HT15-1KT,

USA) according to standard protocols, with final examination by light microscopy.

Hematoxylin & Eosin Staining and Immunohistochemistry

Tissue architecture was evaluated through conventional hematoxylin and eosin (H&E) staining. For immunohistochemical analysis, sections were first treated with 3% hydrogen peroxide for 10 minutes to quench endogenous peroxidase activity. Non-specific binding was blocked with 1% BSA for 1 hour at room temperature. Primary antibody incubation was performed overnight at 4°C, followed by detection using a Rabbit Polymer Detection System (ZSGB-BIO, PV-9000, Beijing, China) according to the manufacturer's instructions. After PBS washes, sections were developed with 3,3'-diaminobenzidine (DAB, ZSGB-BIO, ZLI-9017, Beijing, China) for 2 minutes and counterstained with hematoxylin prior to microscopic evaluation. The following primary antibodies were used: anti-MMP9 (1:200, ab38898, Abcam), anti-CD68 (1:500, ab283654, Abcam), anti-MMP2 (1:200, ab97779, Abcam).

TUNEL Apoptosis Assay

Apoptotic cells were identified in paraffin-embedded sections using a One-Step TUNEL In Situ Apoptosis Kit (Elabscience, E-CK-A321, Wuhan, China) following the manufacturer's protocol. Fluorescent visualization was performed using an epifluorescence microscope equipped with appropriate filters.

RNA Sequencing Analysis

Total RNA was extracted using TRIzol reagent. Library preparation and sequencing were performed by LC-Bio Technologies (Hangzhou, China) using the Illumina NovaSeq 6000 platform.

Raw reads were quality-trimmed (Trimmomatic) and aligned to the reference genome (STAR aligner). Gene expression quantification was performed using featureCounts, followed by differential expression analysis (DESeq2; FDR < 0.05). Functional enrichment was assessed via GO and KEGG pathway analyses (clusterProfiler). Data was uploaded to the Gene Expression Omnibus (GEO) database (GSE290627).

Chromatin Immunoprecipitation Sequencing (ChIP-seq) and ChIP-qPCR

Wild-type (WT) and knockout (KO) cells undergoing differentiation were stimulated with 1 μM

AngII prior to crosslinking. Chromatin was fixed with 1% formaldehyde (v/v) for 10 min at room temperature, followed by quenching with 2.5 M glycine for 5 min. Cells were washed twice with ice-cold PBS, harvested by centrifugation (12,000 × g, 10 min, 4°C), and lysed in RIPA buffer supplemented with protease and phosphatase inhibitors. Chromatin was sheared to 200–500 bp fragments using a Diagenode Bioruptor sonicator (30 sec ON/30 sec OFF cycles, 15 min total).

For immunoprecipitation, lysates were incubated overnight at 4°C with antibodies targeting H3K9me3, H3K9ac, or H3K4me3 (5 μg per reaction), followed by capture with protein A/G magnetic beads. Beads were sequentially washed with: Low-salt buffer (20 mM Tris-HCl pH 8.1, 150 mM NaCl, 2 mM EDTA, 1% Triton X-100, 0.1% SDS), High-salt buffer (500 mM NaCl), LiCl wash buffer (10 mM Tris-HCl pH 8.1, 250 mM LiCl, 1 mM EDTA, 1% deoxycholate, 1% NP-40), TE buffer (10 mM Tris-HCl, 1 mM EDTA, pH 8.0). Immunoprecipitated DNA was eluted (1% SDS, 100 mM NaHCO3, 37°C, 30 min), reverse-crosslinked (200 mM NaCl; RNase A, TransGen, GE101, Beijing, China; 37°C, 30 min), and digested with Proteinase K (TransGen, GE201, Beijing, China, 65°C, 6 h). DNA was purified by phenol-chloroform extraction and ethanol precipitation.

Library preparation and sequencing were performed by LC-Bio Technologies (Hangzhou, China) using the Illumina NovaSeq 6000 platform (150 bp paired-end reads, ~30 million reads/sample). Raw data were processed through standard ChIP-seq pipelines for peak calling (MACS2) and differential binding analysis. Data were uploaded to the Gene Expression Omnibus (GEO) database (GSE296864).

DNA subjected to quantitative qPCR. Primers for ChIP-qPCR were presented in Supplementary Data 4.

Co-immunoprecipitation Assay

HEK293T cells (ATCC, ACS-4500, USA) were co-transfected with pcDNA3.1-*CBX3*-Flag along with one of the following expression plasmids: pcDNA3.1-*RING1*-His, pcDNA3.1-*SUV39H1*-Strep, pcDNA3.1-*HDAC1*-Myc, or pcDNA3.1-*KDM2A*-HA, using Lipofectamine 3000 according to the manufacturer's protocol. After 24 hours, cells were lysed in RIPA buffer (Solarbio, R0010, Beijing, China) containing 1× protease inhibitor cocktail. Lysates were cleared by centrifugation (12,000 × g, 10 min, 4°C), and protein concentrations were determined using a BCA Protein Assay Kit (Thermo Fisher

Scientific, 23225, USA).

For immunoprecipitation, Dynabeads Protein G (Invitrogen, 10004D, USA) were pre-incubated overnight at 4°C with 2 μg of the following antibodies: anti-CBX3, anti-KDM2A, anti-HDAC1, anti-SUV39H1, anti-RING1, or species-matched IgG control. Cleared lysates (500μg total protein) were then incubated with the antibody-conjugated beads overnight at 4°C with gentle rotation.

Following incubation, beads were washed three times with ice-cold RIPA buffer. Bound proteins were eluted by boiling in 2× Laemmli buffer (95°C, 5 min) and analyzed by western blotting as previously described. Input lysates (10% of total) were included as positive controls for all experiments. The list of identified CBX3-interacting proteins is presented in Supplementary Data 5.

Biotin Switch Assay

In vitro sulfhydration.

Approximately 50 mg of mouse liver, or 20 mg aorta tissues was homogenized in HEN buffer (250 mM HEPES–NaOH, Sigma, H3375, USA; 1 mM EDTA, Thermo Fisher Scientific, 15575020, USA; 150 μM deferoxamine, Sigma, d9533, USA; pH 7.7), sonicated, and centrifuged at 12,000×g for 15 min at 4°C. Supernatants were divided into four groups and incubated with H_2O, NaHS (1 mM, Sigma, 161527, USA), DTT (100 mM, Thermo Fisher Scientific, R0861, USA), or NaHS + DTT at 37°C for 1 h. Free thiols were blocked with 20 mM methyl methanethiosulfonate (MMTS, Sigma, 64306, USA) at 50°C for 20 min. Proteins were precipitated with cold acetone (−40°C, 1 h), resuspended in HENS buffer (1% SDS), and labeled with 4 mM biotin-HPDP (Thermo Fisher Scientific, 21341, USA) for 3 h at room temperature. Biotinylated proteins were captured using streptavidin magnetic beads and analyzed by Western blot.

In vivo sulfhydration.

VSMCs or HEK293T cells were treated with NaHS (1 mM) or DTT (2 mM) for 24h. Cell lysates were prepared in RIPA buffer and subjected to immunoprecipitation with anti-CBX3 antibody. Immunoprecipitates were blocked with MMTS and processed according to the biotin switch protocol described above.

Statistical Analysis

All sample sizes are reflected in the figure legends. Data are presented as mean with standard error of the mean (SEM) unless otherwise stated. Differences between two groups were evaluated with unpaired 2-tailed *t*-test (normal distribution), Mann-Whitney test (non-normal distribution), or Fisher's exact test (categorical data). For more groups, data were compared by one-way ANOVA followed by post-hoc analysis. Comparisons including two factors were performed by two-way ANOVA, with repeated measures on the same animals or cells analyzed via two-way mixed-effects ANOVA. All statistical analysis involved using GraphPad Prism v10.1.2. $P<0.05$ was considered statistically significant. No statistical method was used to predetermine sample size. Sample sizes were chosen based on the available number of mice and human data. No data were excluded from the analysis. Mice were randomly assigned to experimental groups matched for genotype, age and body weight. All outcome assessments, including ultrasound and histology, were performed blinded to group allocation to prevent bias. All data were analyzed in a blinded way.

Data Availability

The raw data of bulk RNA-seq data and CHIP-seq generated in this study has been deposited in the NCBI Gene Expression Omnibus (GEO) database under accession code GSE290627 [https://www.ncbi.nlm.nih.gov/geo/query/acc.cgi?acc=GSE290627] and GSE296864 [https://www.ncbi.nlm.nih.gov/geo/query/acc.cgi?acc=GSE296864].

All other data generated and analysed during this study are included in this published article and its supplementary information files. Any additional raw data can be available from the corresponding author upon reasonable request. Source Data are provided with this paper.

References

1. Golledge J. Abdominal aortic aneurysm: update on pathogenesis and medical treatments. *Nat Rev Cardiol* **16**, 225-242 (2019).

2. Cho MJ, Lee MR, Park JG. Aortic aneurysms: current pathogenesis and therapeutic targets. *Exp Mol Med* **55**, 2519-2530 (2023).

3. Lu H*, et al.* Vascular Smooth Muscle Cells in Aortic Aneurysm: From Genetics to Mechanisms. *J Am Heart Assoc* **10**, e023601 (2021).

4. Frantz C, Stewart KM, Weaver VM. The extracellular matrix at a glance. *J Cell Sci* **123**, 4195-4200 (2010).

5. Islam S, Watanabe H. Versican: A Dynamic Regulator of the Extracellular Matrix. *J Histochem Cytochem* **68**, 763-775 (2020).

6. Kemberi M, Salmasi Y, Santamaria S. The Role of ADAMTS Proteoglycanases in Thoracic Aortic Disease. *International Journal of Molecular Sciences* **24**, 12135 (2023).

7. Wight TN. A role for proteoglycans in vascular disease. *Matrix Biol* **71-72**, 396-420 (2018).

8. Yao LY, Moody C, Schonherr E, Wight TN, Sandell LJ. Identification of the proteoglycan versican in aorta and smooth muscle cells by DNA sequence analysis, in situ hybridization and immunohistochemistry. *Matrix Biol* **14**, 213-225 (1994).

9. Cikach FS*, et al.* Massive aggrecan and versican accumulation in thoracic aortic aneurysm and dissection. *JCI Insight* **3**, (2018).

10. Ruiz-Rodríguez MJ*, et al.* Versican accumulation drives Nos2 induction and aortic disease in Marfan syndrome via Akt activation. *EMBO Mol Med* **16**, 132-157 (2024).

11. Santamaria S, de Groot R. ADAMTS proteases in cardiovascular physiology and disease. *Open Biol* **10**, 200333 (2020).

12. Santamaria S*, et al.* Exosites in Hypervariable Loops of ADAMTS Spacer Domains control Substrate Recognition and Proteolysis. *Sci Rep* **9**, 10914 (2019).

13. Minns AF, Qi Y, Yamamoto K, Lee K, Ahnström J, Santamaria S. The C-terminal domains of ADAMTS1 contain exosites involved in its proteoglycanase activity. *J Biol Chem* **299**, 103048 (2023).

14. Ren P*, et al.* ADAMTS-1 and ADAMTS-4 levels are elevated in thoracic aortic aneurysms and dissections. *Ann Thorac Surg* **95**, 570-577 (2013).

15. Ren P, *et al.* Critical Role of ADAMTS-4 in the Development of Sporadic Aortic Aneurysm and Dissection in Mice. *Sci Rep* **7**, 12351 (2017).

16. Zeng T, *et al.* ADAMTS-5 Decreases in Aortas and Plasma From Aortic Dissection Patients and Alleviates Angiotensin II-Induced Smooth Muscle-Cell Apoptosis. *Front Cardiovasc Med* **7**, 136 (2020).

17. Oller J, *et al.* Nitric oxide mediates aortic disease in mice deficient in the metalloprotease Adamts1 and in a mouse model of Marfan syndrome. *Nat Med* **23**, 200-212 (2017).

18. Fava M, *et al.* Role of ADAMTS-5 in Aortic Dilatation and Extracellular Matrix Remodeling. *Arterioscler Thromb Vasc Biol* **38**, 1537-1548 (2018).

19. Yang G, Wang R. H2S and Blood Vessels: An Overview. *Handb Exp Pharmacol* **230**, 85-110 (2015).

20. Gomez I, *et al.* Reverse Regulatory Pathway (H2S / PGE2 / MMP) in Human Aortic Aneurysm and Saphenous Vein Varicosity. *PLoS One* **11**, e0158421 (2016).

21. Luo S, *et al.* Endothelial HDAC1-ZEB2-NuRD Complex Drives Aortic Aneurysm and Dissection Through Regulation of Protein S-Sulfhydration. *Circulation* **147**, 1382-1403 (2023).

22. Zhu J, *et al.* Deficiency of cystathionine gamma-lyase promotes aortic elastolysis and medial degeneration in aged mice. *J Mol Cell Cardiol* **171**, 30-44 (2022).

23. Zhou S, Ma B, Luo M. Matrix metalloproteinases in aortic dissection. *Vascul Pharmacol* **156**, 107420 (2024).

24. Chen Z, *et al.* Vascular smooth muscle cell-derived hydrogen sulfide promotes atherosclerotic plaque stability via TFEB (transcription factor EB)-mediated autophagy. *Autophagy* **18**, 2270-2287 (2022).

25. Oyama K, *et al.* Deletion of HP1γ in cardiac myocytes affects H4K20me3 levels but does not impact cardiac growth. *Epigenetics Chromatin* **11**, 18 (2018).

26. Alam H, *et al.* HP1γ Promotes Lung Adenocarcinoma by Downregulating the Transcription-Repressive Regulators NCOR2 and ZBTB7A. *Cancer Res* **78**, 3834-3848 (2018).

27. Lin Q, *et al.* Cystathionine γ-Lyase Attenuates Vascular Smooth Muscle Cell Senescence via Foxm1-Gas1 Pathway to Mediate Arterial Stiffness. *Antioxidants & redox Signaling* **42**, 655-671 (2025).

28. Jiang S, *et al.* Hydrogen sulphide reduces hyperhomocysteinaemia-induced endothelial ER stress by sulfhydrating protein disulphide isomerase to attenuate atherosclerosis. *J Cell Mol Med* **25**, 3437-3448 (2021).

29. Musto L, Smith A, Pepper C, Bujkiewicz S, Bown M. Risk factor-targeted abdominal aortic aneurysm screening: systematic review of risk prediction for abdominal aortic aneurysm. *British Journal of Surgery* **111**, znae239 (2024).

30. Chi Z*, et al.* Honokiol ameliorates angiotensin II-induced hypertension and endothelial dysfunction by inhibiting HDAC6-mediated cystathionine γ-lyase degradation. *J Cell Mol Med* **24**, 10663-10676 (2020).

31. Bai L*, et al.* Angiotensin II downregulates vascular endothelial cell hydrogen sulfide production by enhancing cystathionine γ-lyase degradation through ROS-activated ubiquitination pathway. *Biochem Biophys Res Commun* **514**, 907-912 (2019).

32. Chi Z*, et al.* Histone deacetylase 6 inhibitor tubastatin A attenuates angiotensin II-induced hypertension by preventing cystathionine γ-lyase protein degradation. *Pharmacol Res* **146**, 104281 (2019).

33. Halper J. Proteoglycans and diseases of soft tissues. *Adv Exp Med Biol* **802**, 49-58 (2014).

34. Wang S*, et al.* Postnatal deficiency of ADAMTS1 ameliorates thoracic aortic aneurysm and dissection in mice. *Exp Physiol* **103**, 1717-1731 (2018).

35. Mizui Y, Yamazaki K, Kuboi Y, Sagane K, Tanaka I. Characterization of 5'-flanking region of human aggrecanase-1 (ADAMTS4) gene. *Mol Biol Rep* **27**, 167-173 (2000).

36. Wang C*, et al.* Epigenetic Up-Regulation of ADAMTS4 in Sympathetic Ganglia is Involved in the Maintenance of Neuropathic Pain Following Nerve Injury. *Neurochem Res* **48**, 2350-2359 (2023).

37. Wu W*, et al.* Cystathionine-γ-lyase ameliorates the histone demethylase JMJD3-mediated autoimmune response in rheumatoid arthritis. *Cell Mol Immunol* **16**, 694-705 (2019).

38. van Wijnen AJ*, et al.* Biological functions of chromobox (CBX) proteins in stem cell self-renewal, lineage-commitment, cancer and development. *Bone* **143**, 115659 (2021).

39. Zhang C*, et al.* Cbx3 inhibits vascular smooth muscle cell proliferation, migration, and neointima formation. *Cardiovasc Res* **114**, 443-455 (2018).

40. Wang G, Xiao Q, Luo Z, Ye S, Xu Q. Functional impact of heterogeneous nuclear ribonucleoprotein A2/B1 in smooth muscle differentiation from stem cells and embryonic arteriogenesis. *J Biol Chem* **287**, 2896-2906 (2012).

41. Wang S*, et al.* Lactate reprograms glioblastoma immunity through CBX3-regulated histone lactylation. *J Clin Invest* **134**, (2024).

42. Wiese M*, et al.* Citrullination of HP1γ chromodomain affects association with chromatin. *Epigenetics Chromatin* **12**, 21 (2019).

43. Cai H*, et al.* LncRNA LINC00998 inhibits the malignant glioma phenotype via the CBX3-mediated c-Met/Akt/mTOR axis. *Cell Death Dis* **11**, 1032 (2020).

44. Vienneau JR, Burns CI, Boghokian A, Soti V. Endovascular Aneurysm Repair Versus Open Surgical Repair in Treating Abdominal Aortic Aneurysm. *Cureus* **16**, e73066 (2024).

45. Bossone E, Eagle KA. Epidemiology and management of aortic disease: aortic aneurysms and acute aortic syndromes. *Nat Rev Cardiol* **18**, 331-348 (2021).

46. Golledge J, Thanigaimani S, Powell JT, Tsao PS. Pathogenesis and management of abdominal aortic aneurysm. *Eur Heart J* **44**, 2682-2697 (2023).

47. Daugherty A, Manning MW, Cassis LA. Angiotensin II promotes atherosclerotic lesions and aneurysms in apolipoprotein E-deficient mice. *J Clin Invest* **105**, 1605-1612 (2000).

48. Lu H, Howatt DA, Balakrishnan A, Graham MJ, Mullick AE, Daugherty A. Hypercholesterolemia Induced by a PCSK9 Gain-of-Function Mutation Augments Angiotensin II-Induced Abdominal Aortic Aneurysms in C57BL/6 Mice-Brief Report. *Arterioscler Thromb Vasc Biol* **36**, 1753-1757 (2016).

49. Kanematsu Y*, et al.* Pharmacologically Induced Thoracic and Abdominal Aortic Aneurysms in Mice. *Hypertension* **55**, 1267-1274 (2010).

Acknowledgments

We thank Professors He Wu and Zengxiang Dong for their help offering human's slices.

Funding

This work was supported by grants from the Natural Science Foundation of China (U24A20650, 82370448, 82100492, 82370315); the State Key Laboratory of Frigid Zone Cardiovascular Diseases, Ministry of Science and Technology, Open Subject (HDHY2024010); the Special project funded by the Ministry of Science and Technology of China (2024GZkf-03); the Key Laboratory of Myocardial Ischemia, Ministry of Education (KF202402) and Heilongjiang Province Spring Swallow Support Project (CYCX24007).

Author Contribution Statement

B.G. designed the study. B.G. and Y.Z. wrote the manuscript. Y.Z. performed most of the in vitro and in vivo experiments. Y.Z., Y.N., and H.G. performed the isolation and culture of mASMCs and replicated the molecular and histological experiments. Y.Z. and H.G. participated in generation of the murine models. B.G. and Y.Z. analyzed the data. H.W. and Z.D. provided the human's slices. L.C., Y.L., H.Z., Y.W. and X.S. critically reviewed and revised the manuscript. B.G., L.Y., Z.C., C.C. and Y.Y. supervised the study and provided the funding. All the authors reviewed and approved the manuscript.

Competing Interests Statement

All authors declare that they have no competing interests.

Figure Legends

Figure 1. Downregulation of CSE in aortic tissues of AAD patients and experimental models. (A) Immunofluorescence analysis of CSE expression in human AAD specimens. Aortic tissues from 15 AAD patients were immunofluorescence stained for CSE (green) and α-smooth muscle actin (α-SMA, magenta; a VSMC marker). Semi-quantitative analysis revealed attenuated CSE expression in the AAD patient's aneurysm region compared to non-AAD patient's aorta tissues. Scale bar: 50 μm. AAD (n=15) and non-AAD (n=10). (B) CSE expression in VSMCs of an AngII-induced AAD model in *Apoe*$^{-/-}$ mice. Immunofluorescence staining demonstrates diminished CSE levels in aneurysmal aortic segments. Scale bar: 50 μm. *Apoe*$^{-/-}$ (n = 8) and *Apoe*$^{-/-}$+Ang II (n = 10). (C, D) Ang II suppresses CSE expression in human aortic smooth muscle cells (HASMCs). HASMCs were treated with AngII (1 μM, 24 h), and *CSE* mRNA (C; quantified by qRT-PCR) and CSE protein levels (D; assessed by Western blot) were significantly downregulated. (n = 6) (E, F) Consistent with human data, (E) AngII treatment attenuated *Cse* mRNA expression in primary mouse aortic smooth muscle cells (mASMCs) (n = 6) (F) AngII treatment attenuated CSE protein expression in primary mouse aortic smooth muscle cells (mASMCs) (n = 5). Data are presented as mean ± SEM. Intergroup differences were evaluated by unpaired two-tailed Student's *t*-test.

Figure 2. VSMCs-specific *Cse* deletion exacerbates AAD incidence and progression.
(A–D) Hypercholesterolemia- and AngII-induced AAD model: VSMCs-specific *Cse* knockout mice (*Cse*^{SMCKO}) and control mice (*Cse*^{LOXP}) were subjected to an AAD model via liver-specific *Pcsk9* overexpression (inducing hypercholesterolemia), Paigen diet feeding, and AngII infusion. After 4 weeks, *Cse*^{SMCKO} mice exhibited aggravated AAD formation and progression compared to controls, as demonstrated by: (A) representative aortic images and AAD incidence rate, *Cse*^{LOXP} mice (n = 25) and *Cse*^{SMCKO} mice (n = 22). (B) survival curve, *Cse*^{LOXP} mice (n = 25) and *Cse*^{SMCKO} mice (n = 22). (C) aortic diameter measured by ultrasound (n = 12). (D) Elastin degradation assessed by H&E and Elastin staining (grading scale shown) *Cse*^{LOXP} mice (n = 12) and *Cse*^{SMCKO} mice (n = 14). (E–H) BAPN plus AngII-induced AAA model for phenotypic validation: consistent with the first model, *Cse*^{SMCKO} mice displayed heightened AAD severity compared to *Cse*^{LOXP} mice, including: (E) increased AAA incidence, *Cse*^{LOXP} mice (n = 29) and *Cse*^{SMCKO} mice (n = 23). (F) elevated mortality, *Cse*^{LOXP} mice (n = 29) and *Cse*^{SMCKO} mice (n = 23). (G) expanded aortic diameter, *Cse*^{LOXP} mice (n = 14) and *Cse*^{SMCKO} mice (n = 8). (H) enhanced elastin degradation (n = 11). Data are presented as mean ± SEM. Kolmogorov-Smirnov test for data normality and unpaired two-tailed Student's *t*-test for intergroup difference were used. Mantel-Cox test was used for survival curve analysis.

Figure 3. VSMCs-specific *Cse* deletion promotes ADAMTS4 accumulation and versican degradation. (A) Heatmap of RNA-seq analysis showing differential expression of ADAM family genes in cultured primary *Cse*-knockout (KO) and wild-type (WT) VSMCs treated with AngII (1 μM, 24 h). *$P < 0.05$ (n = 5). (B) qRT-PCR validation confirmed significant upregulation of *Adamts4* in *Cse*-knockout (KO) VSMCs, WT and KO (n = 5), WT + Ang II and KO + Ang II (n = 6). (C) Western blot analysis revealed elevated ADAMTS4 protein levels and enhanced versican degradation in *Cse*-knockout (KO) VSMCs (n = 6). (D) Conversely, *Cse* overexpression in VSMCs suppressed ADAMTS4 expression (n = 6) and attenuated versican cleavage (n = 5). (E) In vivo, ADAMTS4 protein was elevated in aortic VSMCs from

Cse^{SMCKO} mice compared to *Cse*^{LOXP} controls in two AngII-induced AAD models, *Cse*^{LOXP} mice +AAV8-*Pcsk9* +Ang II (n = 5) and *Cse*^{SMCKO} mice +AAV8-*Pcsk9* +Ang II (n = 4), *Cse*^{LOXP} mice + BAPN+Ang II (n = 8) and *Cse*^{SMCKO} mice + BAPN+Ang II (n = 8), and the versican cleavage product (V1) was elevated in aortic VSMCs from *Cse*^{SMCKO} mice compared to *Cse*^{LOXP} controls in two AngII-induced AAD models, *Cse*^{LOXP} mice + AAV8-*Pcsk9* + Ang II (n = 6) and *Cse*^{SMCKO} mice + AAV8-*Pcsk9* + Ang II (n = 7), *Cse*^{LOXP} mice + BAPN+Ang II (n = 5) and *Cse*^{SMCKO} mice + BAPN+Ang II (n = 5). (F) Increased ADAMTS4 expression was also observed in human AAD tissues, AAD (n = 15) and non-AAD (n = 10). (G) In AngII-induced *Apoe*$^{-/-}$ AAD aorta, ADAMTS4 accumulation , *Apoe*$^{-/-}$ (n = 9) and *Apoe*$^{-/-}$+Ang II (n = 8), correlated with versican V1 deposition, *Apoe*$^{-/-}$ (n = 6) and *Apoe*$^{-/-}$+Ang II (n = 7). (E-F) ADAMTS4 (green) and α-SMA (magenta). Data are presented as mean ± SEM. For two-factor comparisons (*Cse* overexpression and AngII treatment), two-way mixed-effects ANOVA followed by Tukey's multiple comparisons test was applied. Other two-group comparisons were analyzed by unpaired two-tailed Student's *t*-test.

Figure 4. CSE downregulates ADAMTS4 in a CBX3-dependent manner. (A) Heatmap showing alterations in PRC1 and PRC2 gene expression in RNA-seq analysis of *Cse*-knockout (KO) VSMCs. **P* < 0.05 indicates significantly downregulated genes (n = 5). CBX3 protein expression was attenuated in *Cse*-deficient VSMCs, as confirmed by Western blot (n = 6) (B) and immunofluorescence staining (n = 4) (C). Conversely, *Cse* overexpression upregulated CBX3 protein levels (n = 5) (D). Consistent with these findings, CBX3 expression was also diminished in aortic VSMCs from two distinct *Cse*^{SMCKO} AAD mouse models, *Cse*^{LOXP} mice + AAV8-*Pcsk9* +Ang II (n = 5) and *Cse*^{SMCKO} mice + AAV8-*Pcsk9* +Ang II (n = 5), *Cse*^{LOXP} mice + BAPN+Ang II (n = 11) and *Cse*^{SMCKO} mice + BAPN+Ang II (n = 12), (E), as well as in human AAD tissues, AAD (n = 15) and non-AAD (n = 10) and *Apoe*$^{-/-}$ AAD models, *Apoe*$^{-/-}$ (n = 7) and Apoe$^{-/-}$+Ang II (n = 9). (C, E, F) CBX3 (green) and α-SMA (magenta). (F). Genetic knockdown of *Cbx3* via siRNA in primary *Cse*-knockout (KO) VSMCs exacerbated ADAMTS4 upregulation and versican cleavage (Mean ± SEM; n = 6) (G), whereas *Cbx3* overexpression rescued ADAMTS4 induction (n = 6) and versican degradation (n = 5) caused by *Cse* deficiency (H). Data are presented as mean ± SEM. Data in (D) and (H) were analyzed by two-way mixed-effects ANOVA followed by Tukey's multiple comparisons test; all other panels were assessed using an unpaimagenta two-tailed Student's *t*-test.

Figure 5. Local *Cbx3* overexpression rescues BAPN/AngII-induced AAD in *Cse*^{SMCKO} mice via AAV9-mediated gene delivery. An absorbable collagen sponge-based extravascular carrier, loaded with AAV9-sm22α-*Cbx3*, was implanted around the abdominal aorta (between the diaphragm and renal artery) to achieve smooth muscle cell-specific *Cbx3* overexpression. Local *Cbx3* restoration attenuated AAD formation in *Cse*^{SMCKO} mice, as demonstrated by: (A) Representative aortic images, (B) attenuated AAD incidence (n = 14), and (C) suppressed aortic dilation, AAV9-*GFP* (n = 14) and AAV9-*Cbx3* (n = 11). Histological and molecular analyses further revealed that *Cbx3* overexpression mitigated (D) elastin degradation and collagen deposition (n = 13), (E) versican (V1) accumulation, AAV9-*GFP* (n = 7) and AAV9-*Cbx3* (n = 8)., (F) ADAMTS4 upregulation (n = 6) and CBX3 overexpression, AAV9-*GFP* (n = 6) and AAV9-*Cbx3* (n = 5), (the upper two panels) ADAMTS4 (green) and α-SMA (magenta). (the bottom two panels) CBX3 (green) and α-SMA (magenta). (G) VSMC apoptosis AAV9-*GFP* (n = 9) and AAV9-*Cbx3* (n = 10), and (H) macrophage infiltration, AAV9-*GFP* (n = 7) and AAV9-*Cbx3* (n = 8), and

attenuated MMP2 expression, AAV9-*GFP* (n = 10) and AAV9-*Cbx3* (n = 7), and attenuated MMP9 expression, AAV9-*GFP* (n = 9) and AAV9-*Cbx3* (n = 5). Data are presented as mean ± SEM. Statistical analysis: Unpaired two-tailed Student's *t*-test.

Figure 6. CSE regulates histone modifications via CBX3 and profiling histone modifications in *Cse*-deficient VSMCs. (A) Western blot analysis of primary *Cse*-knockout VSMCs revealed attenuated methylation (me3) and acetylation (ac) of H3K9 and H3K4 following stimulation with AngII or ox-LDL, whereas H3K27 methylation remained unchanged (n = 6). (B) Conversely, *Cse* overexpression increased H3K9me3, H3K9ac, H3K4me3, and H3K4ac levels but did not affect H3K27me3, as demonstrated by western blot (n =6). (C) Immunofluorescence staining confirmed decreased H3K9me3 expression in aortic tissues from the AngII-induced AAD models with VSMC-specific *Cse* knockout (Cse^{SMCKO} mice), Cse^{LOXP} mice + AAV8-*Pcsk9*+Ang II (n = 10) and Cse^{SMCKO} mice + AAV8-*Pcsk9* +Ang II (n = 11), Cse^{LOXP} mice + BAPN+Ang II (n = 12) and Cse^{SMCKO} mice + BAPN+Ang II (n = 10), and Immunofluorescence staining confirmed decreased H3K9ac expression in aortic tissues from the AngII-induced AAD models with VSMC-specific *Cse* knockout (Cse^{SMCKO} mice), Cse^{LOXP} mice + AAV8-*Pcsk9* +Ang II (n = 9) and Cse^{SMCKO} mice + AAV8-*Pcsk9* +Ang II (n = 8), Cse^{LOXP} mice + BAPN+Ang II (n = 11) and Cse^{SMCKO} mice + BAPN+Ang II (n = 10), (the upper four panels) H3K9me3 (green) and α-SMA (magenta), (the bottom four panels) H3K9ac (green) and α-SMA (magenta). (D) Similarly, immunofluorescence staining showed attenuated H3K4me3 expression in aortic tissues from two AngII-induced AAD models following *Cse* deletion in VSMCs, Cse^{LOXP} mice + AAV8-*Pcsk9* +Ang II (n = 9) and Cse^{SMCKO} mice + AAV8-*Pcsk9* +Ang II (n = 7), Cse^{LOXP} mice + BAPN+Ang II (n = 10) and Cse^{SMCKO} mice + BAPN+Ang II (n = 10), and immunofluorescence staining showed attenuated H3K4ac expression in aortic tissues from two AngII-induced AAD models following *Cse* deletion in VSMCs, Cse^{LOXP} mice + AAV8-*Pcsk9* +Ang II (n = 6) and Cse^{SMCKO} mice + AAV8-*Pcsk9* +Ang II (n = 6), Cse^{LOXP} mice + BAPN+Ang II (n = 9) and Cse^{SMCKO} mice + BAPN+Ang II (n = 6), (the upper four panels) H3K4me3 (green) and α-SMA (magenta), (the bottom four panels) H3K4ac (green) and α-SMA (magenta). (E) Western blot analysis of *Cse*-knockout VSMCs demonstrated that *Cbx3* knockdown further diminished H3K9me3/ac and H3K4me3/ac protein expression. No significant alteration was observed in H3K27me3 expression. (n = 6). (F) Overexpression of *Cbx3* rescued the downregulation of H3K9me3/ac and H3K4me3/ac induced by *Cse* deletion, H3K9/4me3 (n = 6), H3K9/4ac (n = 5). No significant alteration was observed in H3K27me3 expression (n = 5). Data are presented as mean ± SEM. Data in (B) and (F) were analyzed by two-way mixed-effects ANOVA followed by Tukey's multiple comparisons test. All other panels were analyzed using an unpaimagenta two-tailed Student's *t*-test.

Figure 7. Profiling histone modifications in *Cse*-deficient VSMCs. (A) Analysis of H3K9me3 in WT vs. KO VSMCs (n = 3). Upper panel: Heatmap of H3K9me3 enrichment. Middle panel: Average ChIP-seq signal profiles. Lower panel: Venn diagram depicting overlaps between H3K9me3-target genes and differentially expressed genes from RNA-seq. Right panel: GO enrichment analysis of overlapping genes. (B) Integrated analysis of H3K9ac ChIP-seq and RNA-seq, with GO enrichment of overlapping genes (n = 3). (C) Integrated analysis of H3K4me3 ChIP-seq and RNA-seq, with GO enrichment of overlapping genes (n = 3). (D & E) IGV tracks displaying ChIP-seq signals for H3K9me3, H3K9ac, and H3K4me3 at key genes: (D) ECM remodeling-related genes (*Adamts4*, *Mmp9*) (n = 3), (E) *Col1a2* (ECM-associated

gene) (n = 3), Inflammatory gene *Nlrp3* (n = 3), Apoptosis-related gene *Bcl2* (n = 3). Statistical analysis: Data are presented as mean ± SEM.

Figure 8. CBX3 forms an epigenetic complex with partner proteins. (A) Validation of CBX3-protein interactions in HEK293T cells. Plasmids encoding Flag-tagged *CBX3*, HA-tagged *KDM2A*, Myc-tagged *HDAC1*, His-tagged *RING1*, and Strep-tagged *SUV39H1* were co-transfected in pairwise combinations. Protein interactions were assessed by Co-IP using tag-specific antibodies. (B) Co-IP confirmation of endogenous CBX3-protein interactions in primary VSMCs. (C) Disruption of CBX3 interactions with SUV39H1, KDM2A, and HDAC1 in *Cse*-deficient VSMCs (n = 3). Data represent mean ± SEM; significance was determined by unpaimagenta two-tailed Student's *t*-test.

Figure 9. CBX3 sulfhydration inhibits ubiquitin-mediated degradation of CBX3. In vitro sulfhydration of CBX3 was assessed by biotin-switch assay in liver homogenates (A) and aortic homogenates (B) following treatment with the H_2S donor NaHS (1 mM) or the reducing agent DTT (100 mM). In VSMCs, cells were treated with NaHS (1 mM) or DTT (2 mM), followed by immunoprecipitation with anti-CBX3 antibody; CBX3 sulfhydration was then detected by biotin-switch assay (C). Endogenous CBX3 sulfhydration was further evaluated in *Cse*-deficient VSMCs (D), (n = 3), after AngII treatment, (n = 3) (E), and following restoration with the CSE activator noswertianolin, (n = 3) (F). Site-directed mutagenesis of C69, C160, and C177 was performed to determine their roles in CBX3 sulfhydration and in CBX3-mediated regulation of H3K9me3 and H3K9ac (G), with quantitative analysis shown in (H), (n = 4) . AngII-induced CBX3 degradation in VSMCs is shown in (I), (n = 3). NaHS or noswertianolin attenuated AngII-induced CBX3 degradation (J), (n = 5) . HEK-293T cells were transfected with wild-type or cysteine-mutant *Cbx3* plasmids to assess the effect of NaHS on CBX3 stability (n = 5) (K). Transfect HEK-293T cells and VSMCs with wild-type or cysteine-mutant *CBX3* plasmids, and evaluate the effect of NaHS on CBX3 stability by immunofluorescence, CBX3 (green) and α-SMA (magenta) (L).

Data are presented as mean ± SEM. (D-F) unpaired two-tailed Student's *t*-test.; (H-K) one-way ANOVA followed by Tukey's multiple-comparisons test.

Figure 10. Local overexpression of *Cse* or *Cbx3* via an extravascular carrier attenuates AAD incidence and progression. (A-E) A collagen-based absorbable extravascular carrier was implanted on the abdominal aorta and loaded with AAV9-sm22α-*Cse* or AAV9-sm22α-*Cbx3* to achieve localized overexpression of *Cse* or *Cbx3* in the aortic wall. This intervention mitigated AngII-induced AAD formation and progression in *Apoe*$^{-/-}$ mice, as evidenced by: (A) Representative aortic images and incidence rate of AAD (n = 12). (B) attenuated abdominal aortic diameter (n = 12). (C) Attenuated elastin degradation (n = 12). (D) Decreased ADAMTS4 accumulation and CBX3 overexpression (n = 12), (the upper two panels) ADAMTS4 (green) and α-SMA (magenta). (the bottom two panels) CBX3 (green) and α-SMA (magenta). (E) Suppressed versican cleavage (n = 10). Data are presented as mean ± SEM. Statistical significance was determined by one-way ANOVA followed by Dunnett's multiple comparisons test.

Editorial summary:

Aortic aneurysm and dissection are life-threatening conditions primarily managed surgically. Here, the authors showed that CSE/H_2S exerts protective effects by sulfhydrating and stabilizing CBX3, and modulating histone modification.

Peer review information: *Nature Communications* thanks the anonymous, reviewer(s) for their contribution to the peer review of this work. A peer review file is available.

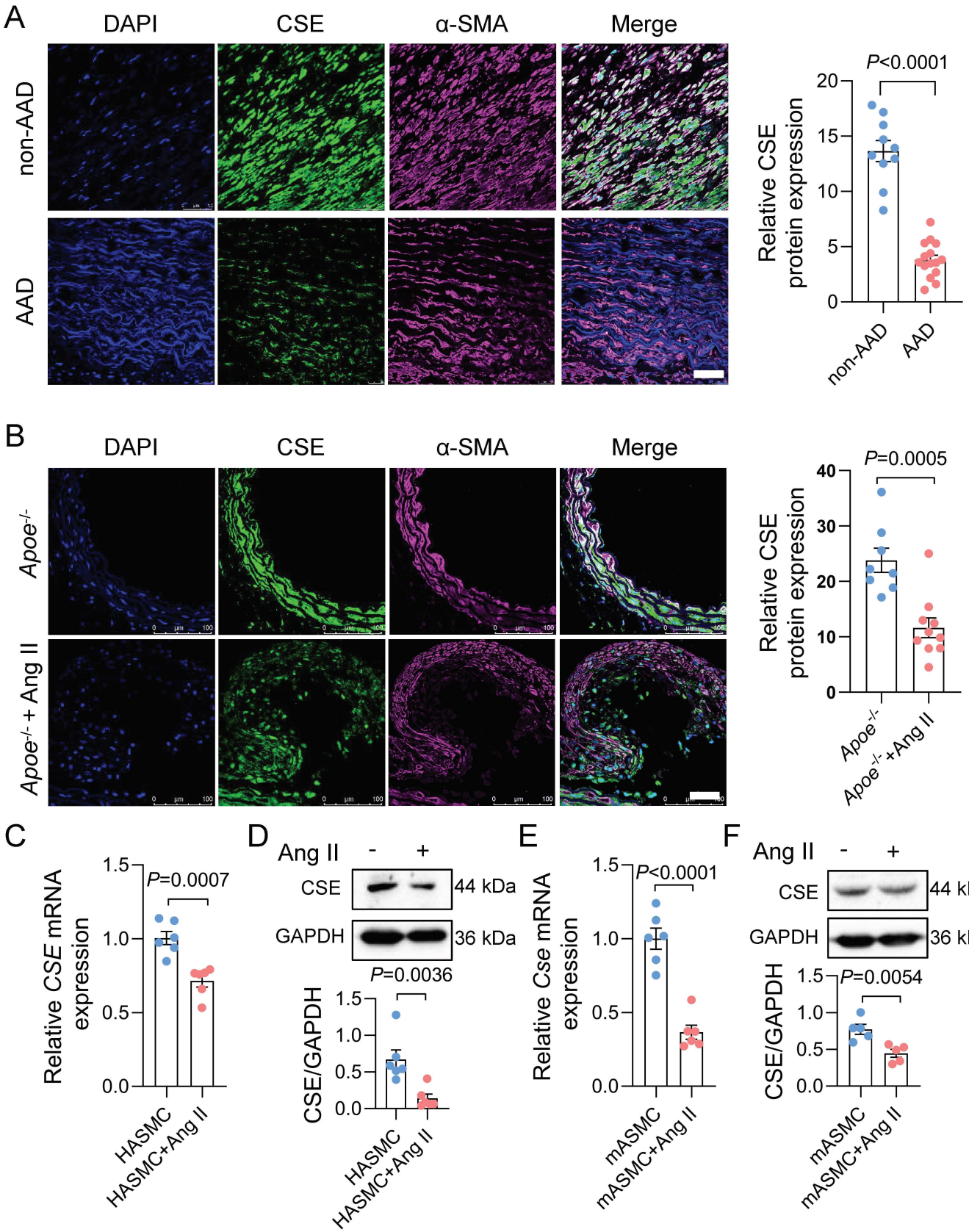
A
DAPI
CSE
α-SMA
Merge
non-AAD
AAD
Relative CSE protein expression
P<0.0001
non-AAD
AAD
B
DAPI
CSE
α-SMA
Merge
Apoe-/-
Apoe-/- + Ang II
Relative CSE protein expression
P=0.0005
Apoe-/-
Apoe-/- +Ang II
C
Relative CSE mRNA expression
P=0.0007
HASMC
HASMC+Ang II
D
Ang II - +
CSE
44 kDa
GAPDH
36 kDa
P=0.0036
CSE/GAPDH
HASMC
HASMC+Ang II
E
Relative Cse mRNA expression
P<0.0001
mASMC
mASMC+Ang II
F
Ang II - +
CSE
44 kDa
GAPDH
36 kDa
P=0.0054
CSE/GAPDH
mASMC
mASMC+Ang II

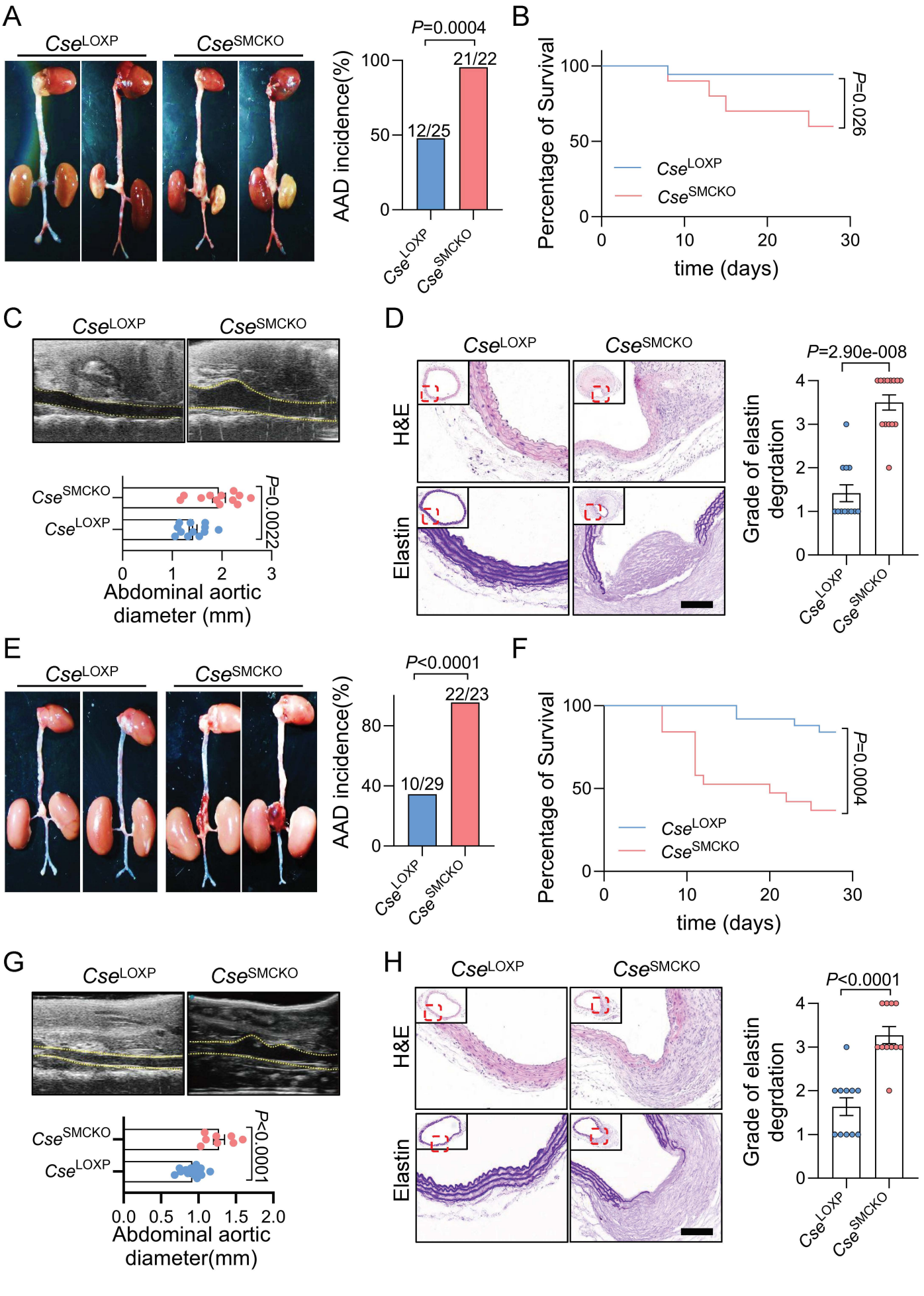
A
Cse^LOXP
Cse^SMCKO
P=0.0004
AAD incidence(%)
100
50
0
12/25
21/22
Cse^LOXP
Cse^SMCKO
B
Percentage of Survival
100
50
0
P=0.026
Cse^LOXP
Cse^SMCKO
0
10
20
30
time (days)
C
Cse^LOXP
Cse^SMCKO
Cse^SMCKO
Cse^LOXP
P=0.0022
0
1
2
3
Abdominal aortic diameter (mm)
D
Cse^LOXP
Cse^SMCKO
H&E
Elastin
P=2.90e-008
Grade of elastin degrdation
4
3
2
1
0
Cse^LOXP
Cse^SMCKO
E
Cse^LOXP
Cse^SMCKO
P<0.0001
AAD incidence(%)
80
40
0
10/29
22/23
Cse^LOXP
Cse^SMCKO
F
Percentage of Survival
100
50
0
P=0.0004
Cse^LOXP
Cse^SMCKO
0
10
20
30
time (days)
G
Cse^LOXP
Cse^SMCKO
Cse^SMCKO
Cse^LOXP
P<0.0001
0.0
0.5
1.0
1.5
2.0
Abdominal aortic diameter(mm)
H
Cse^LOXP
Cse^SMCKO
H&E
Elastin
P<0.0001
Grade of elastin degrdation
4
3
2
1
0
Cse^LOXP
Cse^SMCKO

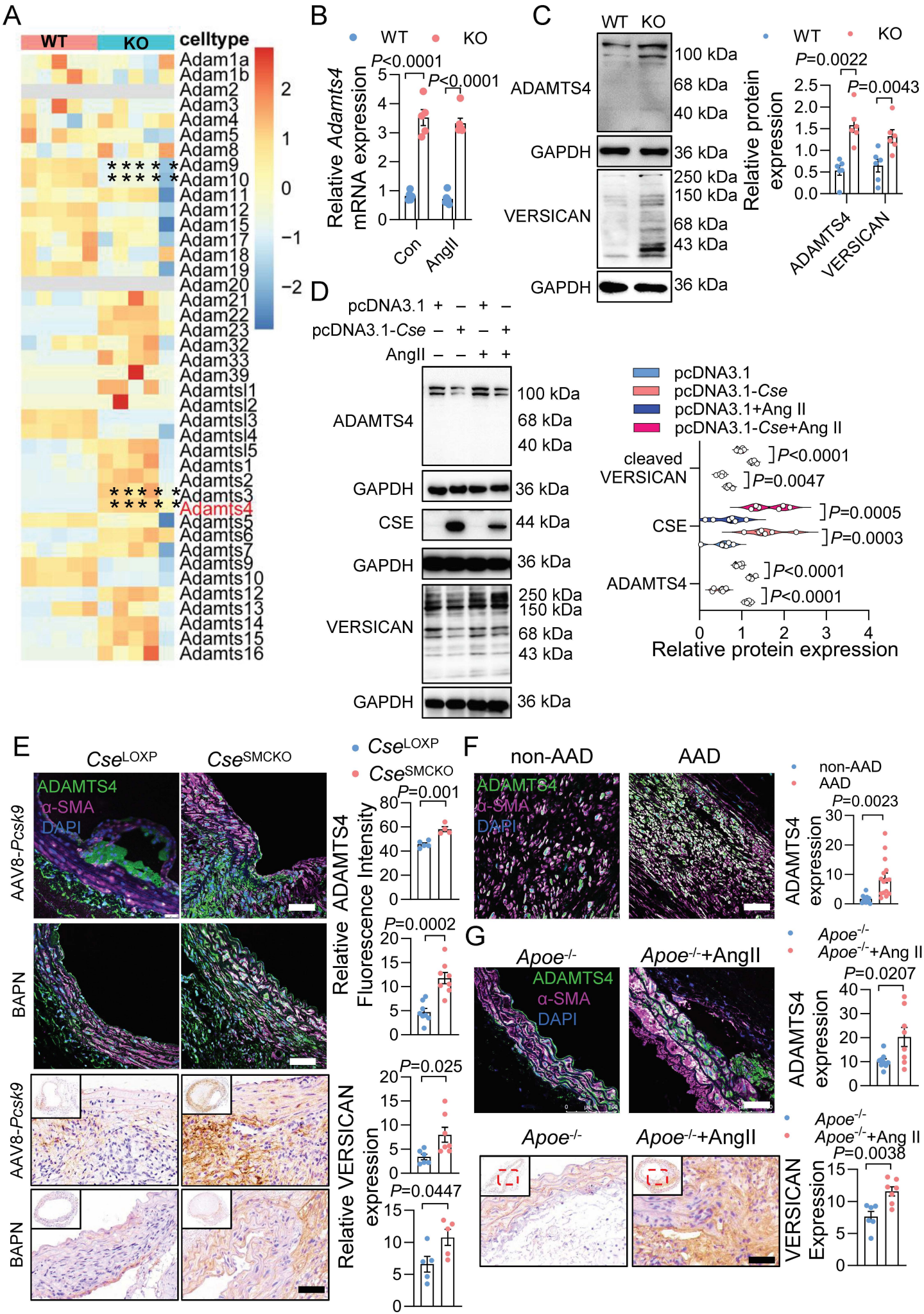
A
WT
KO
celltype
Adam1a
Adam1b
Adam2
Adam3
Adam4
Adam5
Adam8
Adam9
Adam10
Adam11
Adam12
Adam15
Adam17
Adam18
Adam19
Adam20
Adam21
Adam22
Adam23
Adam32
Adam33
Adam39
Adamtsl1
Adamtsl2
Adamtsl3
Adamtsl4
Adamtsl5
Adamts1
Adamts2
Adamts3
Adamts4
Adamts5
Adamts6
Adamts7
Adamts9
Adamts10
Adamts12
Adamts13
Adamts14
Adamts15
Adamts16
2
1
0
−1
−2
B
WT
KO
P<0.0001
P<0.0001
Relative Adamts4 mRNA expression
Con
AngII
C
WT
KO
ADAMTS4
GAPDH
VERSICAN
GAPDH
100 kDa
68 kDa
40 kDa
36 kDa
250 kDa
150 kDa
68 kDa
43 kDa
36 kDa
Relative protein expression
P=0.0022
P=0.0043
ADAMTS4
VERSICAN
D
pcDNA3.1
pcDNA3.1-Cse
AngII
ADAMTS4
GAPDH
CSE
GAPDH
VERSICAN
GAPDH
100 kDa
68 kDa
40 kDa
36 kDa
44 kDa
36 kDa
250 kDa
150 kDa
68 kDa
43 kDa
36 kDa
pcDNA3.1
pcDNA3.1-Cse
pcDNA3.1+Ang II
pcDNA3.1-Cse+Ang II
cleaved VERSICAN
CSE
ADAMTS4
P<0.0001
P=0.0047
P=0.0005
P=0.0003
P<0.0001
P<0.0001
Relative protein expression
E
CseLOXP
CseSMCKO
AAV8-Pcsk9
BAPN
ADAMTS4
α-SMA
DAPI
CseLOXP
CseSMCKO
P=0.001
Relative ADAMTS4 Fluorescence Intensity
P=0.0002
P=0.025
Relative VERSICAN expression
P=0.0447
F
non-AAD
AAD
ADAMTS4
α-SMA
DAPI
non-AAD
AAD
P=0.0023
ADAMTS4 expression
G
Apoe-/-
Apoe-/-+AngII
ADAMTS4
α-SMA
DAPI
Apoe-/-
Apoe-/-+Ang II
P=0.0207
ADAMTS4 expression
Apoe-/-
Apoe-/-+AngII
Apoe-/-
Apoe-/-+Ang II
P=0.0038
VERSICAN Expression

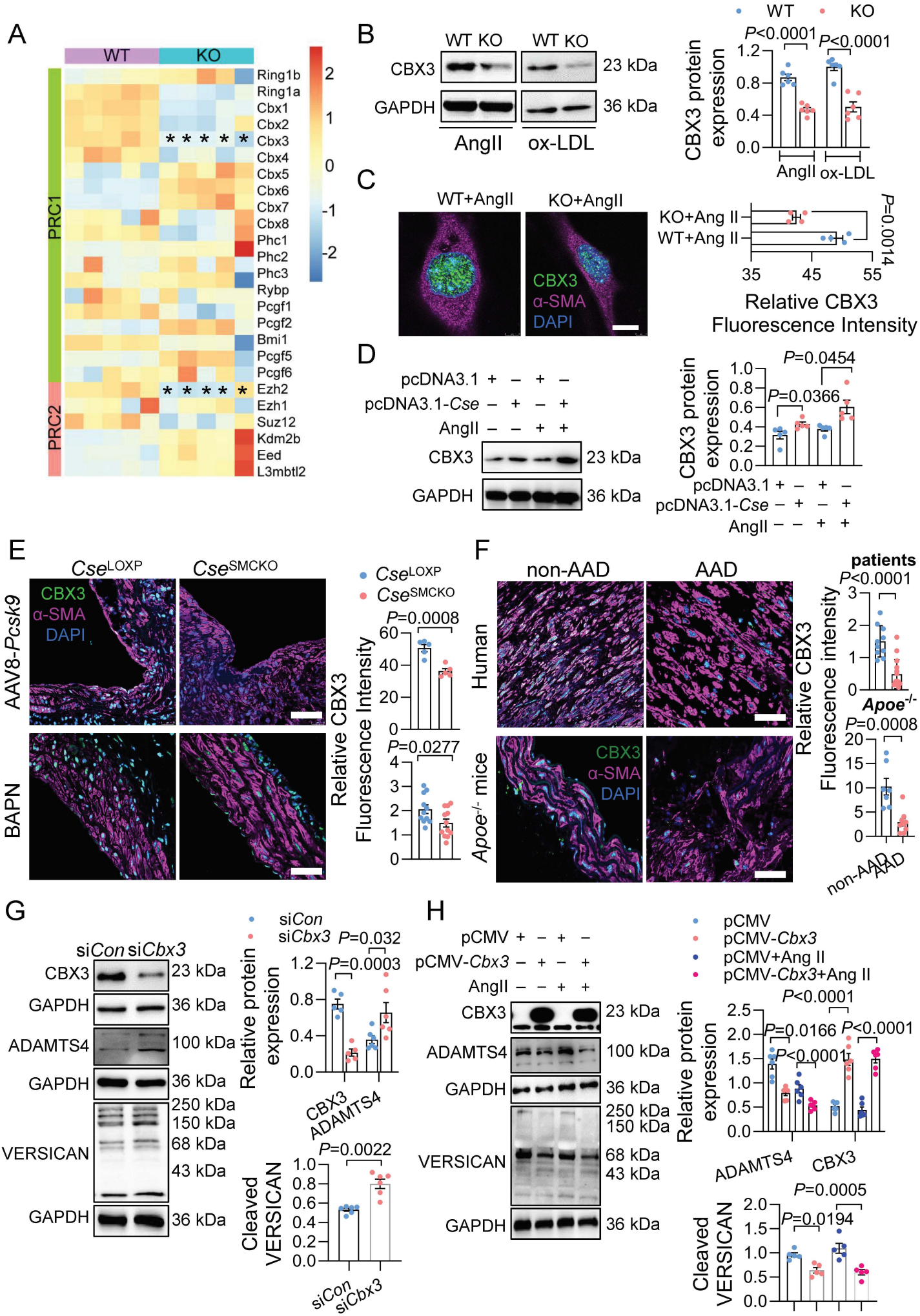
A
WT
KO
PRC1
PRC2
Ring1b
Ring1a
Cbx1
Cbx2
Cbx3
Cbx4
Cbx5
Cbx6
Cbx7
Cbx8
Phc1
Phc2
Phc3
Rybp
Pcgf1
Pcgf2
Bmi1
Pcgf5
Pcgf6
Ezh2
Ezh1
Suz12
Kdm2b
Eed
L3mbtl2
2
1
0
-1
-2
B
WT KO
WT KO
CBX3
GAPDH
23 kDa
36 kDa
AngII
ox-LDL
WT
KO
P<0.0001
P<0.0001
CBX3 protein expression
AngII
ox-LDL
C
WT+AngII
KO+AngII
CBX3
α-SMA
DAPI
KO+Ang II
WT+Ang II
P=0.0014
Relative CBX3 Fluorescence Intensity
D
pcDNA3.1
pcDNA3.1-Cse
AngII
CBX3
GAPDH
23 kDa
36 kDa
P=0.0454
P=0.0366
CBX3 protein expression
E
CseLOXP
CseSMCKO
AAV8-Pcsk9
BAPN
CBX3
α-SMA
DAPI
P=0.0008
P=0.0277
Relative CBX3 Fluorescence Intensity
F
non-AAD
AAD
Human
Apoe-/- mice
CBX3
α-SMA
DAPI
patients
P<0.0001
Apoe-/-
P=0.0008
Relative CBX3 Fluorescence intensity
non-AAD
AAD
G
siCon
siCbx3
CBX3
GAPDH
ADAMTS4
VERSICAN
23 kDa
36 kDa
100 kDa
250 kDa
150 kDa
68 kDa
43 kDa
P=0.032
P=0.0003
Relative protein expression
CBX3
ADAMTS4
P=0.0022
Cleaved VERSICAN
H
pCMV
pCMV-Cbx3
AngII
P<0.0001
P=0.0166
P<0.0001
P<0.0001
Relative protein expression
ADAMTS4
CBX3
P=0.0005
P=0.0194
Cleaved VERSICAN

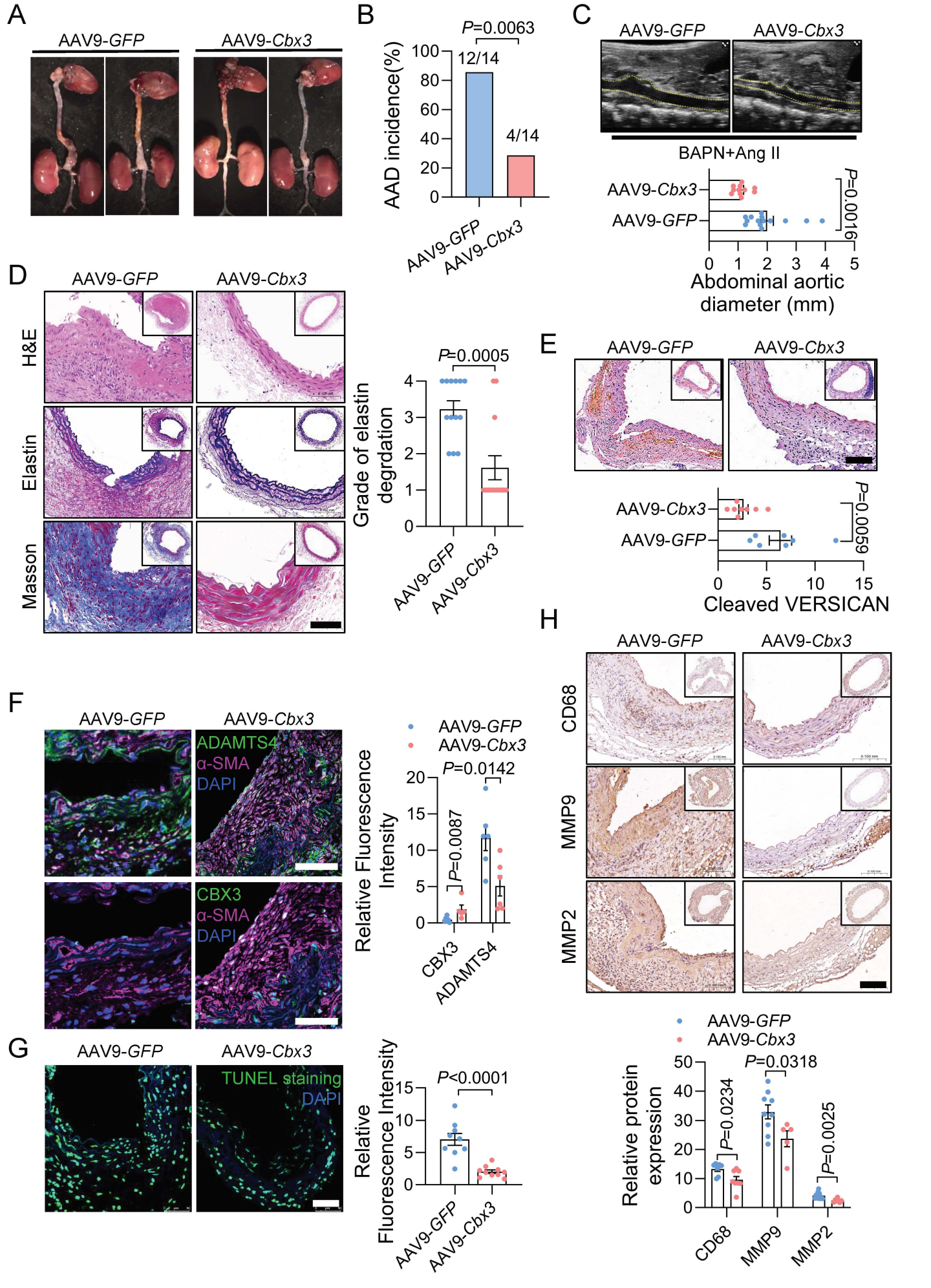
A
AAV9-GFP
AAV9-Cbx3
B
P=0.0063
12/14
4/14
AAD incidence(%)
AAV9-GFP
AAV9-Cbx3
C
AAV9-GFP
AAV9-Cbx3
BAPN+Ang II
AAV9-Cbx3
AAV9-GFP
P=0.0016
Abdominal aortic diameter (mm)
D
AAV9-GFP
AAV9-Cbx3
H&E
Elastin
Masson
P=0.0005
Grade of elastin degrdation
E
AAV9-GFP
AAV9-Cbx3
AAV9-Cbx3
AAV9-GFP
P=0.0059
Cleaved VERSICAN
F
AAV9-GFP
AAV9-Cbx3
ADAMTS4
α-SMA
DAPI
CBX3
α-SMA
DAPI
AAV9-GFP
AAV9-Cbx3
P=0.0142
P=0.0087
Relative Fluorescence Intensity
CBX3
ADAMTS4
G
AAV9-GFP
AAV9-Cbx3
TUNEL staining
DAPI
P<0.0001
Relative Fluorescence Intensity
AAV9-GFP
AAV9-Cbx3
H
AAV9-GFP
AAV9-Cbx3
CD68
MMP9
MMP2
AAV9-GFP
AAV9-Cbx3
P=0.0318
P=0.0234
P=0.0025
Relative protein expression
CD68
MMP9
MMP2

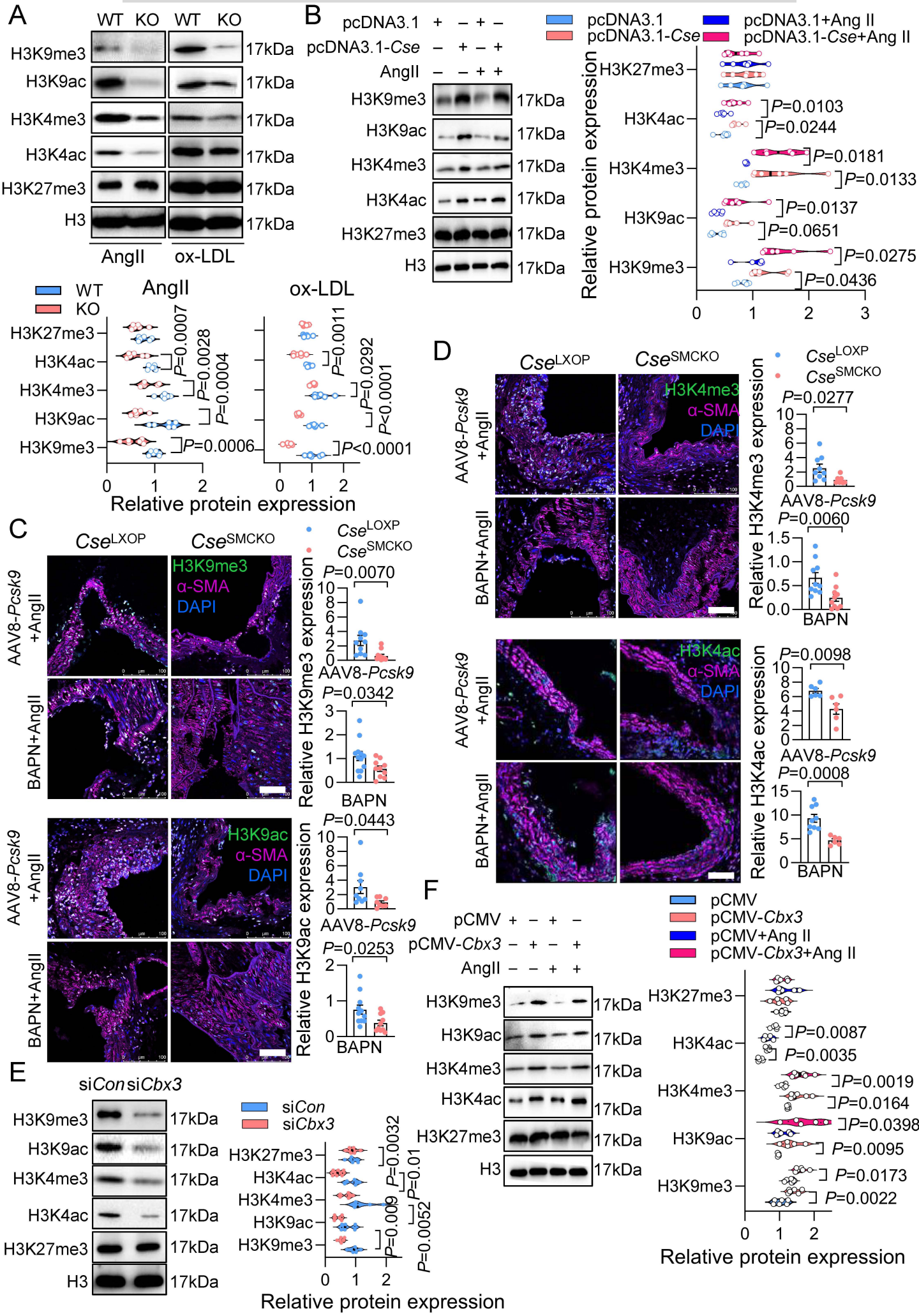
A
WT KO WT KO
H3K9me3
H3K9ac
H3K4me3
H3K4ac
H3K27me3
H3
17kDa
AngII
ox-LDL
B
pcDNA3.1 + – + –
pcDNA3.1-Cse – + – +
AngII – – + +
pcDNA3.1
pcDNA3.1-Cse
pcDNA3.1+Ang II
pcDNA3.1-Cse+Ang II
Relative protein expression
P=0.0103
P=0.0244
P=0.0181
P=0.0133
P=0.0137
P=0.0651
P=0.0275
P=0.0436
WT
KO
AngII
ox-LDL
P=0.0007
P=0.0028
P=0.0004
P=0.0006
P=0.0011
P=0.0292
P<0.0001
P<0.0001
C
CseLXOP
CseSMCKO
AAV8-Pcsk9 +AngII
BAPN+AngII
H3K9me3
α-SMA
DAPI
Relative H3K9me3 expression
P=0.0070
AAV8-Pcsk9
P=0.0342
BAPN
H3K9ac
Relative H3K9ac expression
P=0.0443
AAV8-Pcsk9
P=0.0253
BAPN
D
H3K4me3
H3K4ac
Relative H3K4me3 expression
P=0.0277
AAV8-Pcsk9
P=0.0060
BAPN
Relative H3K4ac expression
P=0.0098
AAV8-Pcsk9
P=0.0008
BAPN
E
siCon siCbx3
siCon
siCbx3
P=0.0032
P=0.01
P=0.009
P=0.0052
Relative protein expression
F
pCMV + – + –
pCMV-Cbx3 – + – +
AngII – – + +
pCMV
pCMV-Cbx3
pCMV+Ang II
pCMV-Cbx3+Ang II
P=0.0087
P=0.0035
P=0.0019
P=0.0164
P=0.0398
P=0.0095
P=0.0173
P=0.0022
Relative protein expression

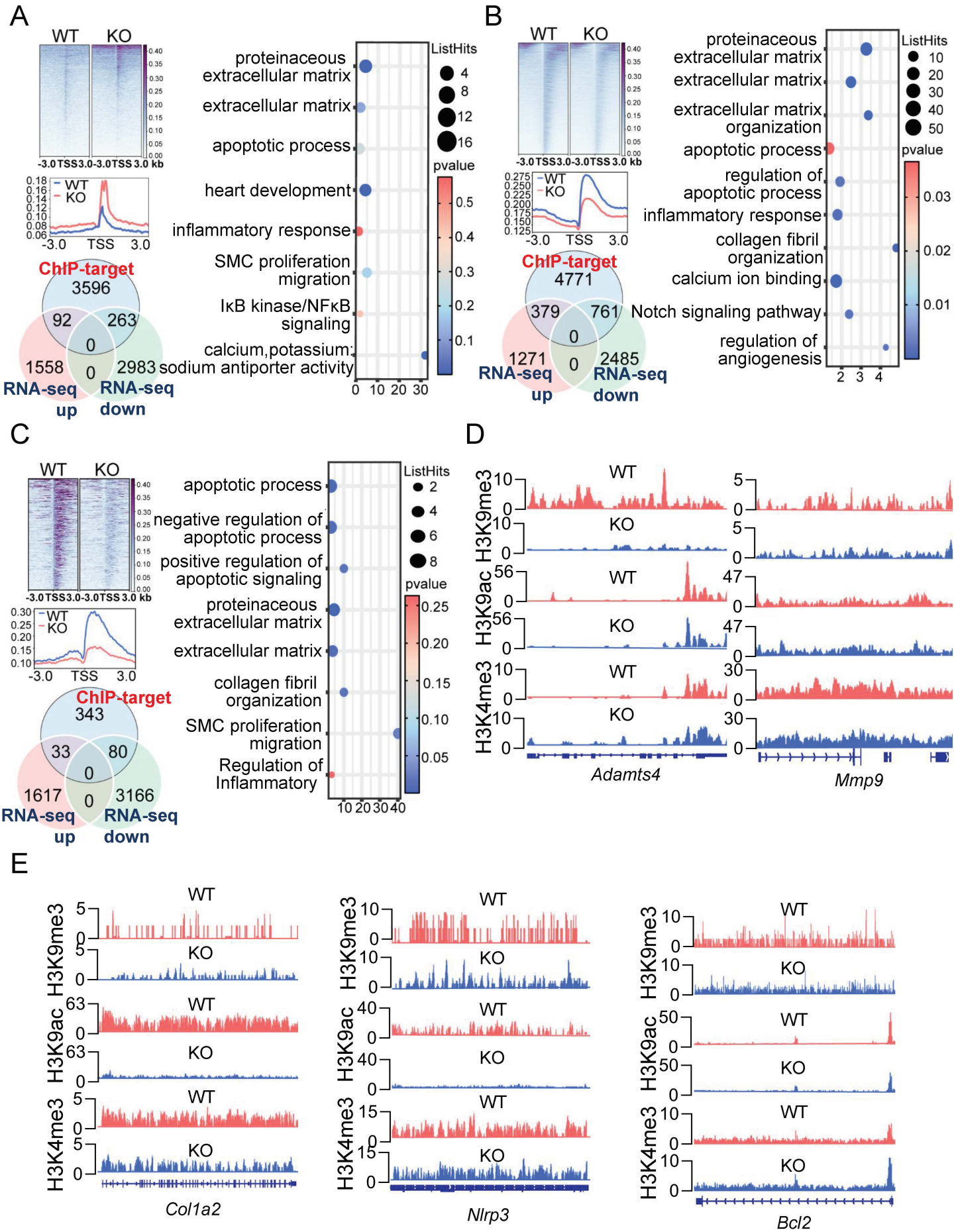
A
WT
KO
-3.0 TSS 3.0 -3.0 TSS 3.0 kb
WT
KO
-3.0 TSS 3.0
ChIP-target
3596
92
263
0
1558
0
2983
RNA-seq up
RNA-seq down
proteinaceous extracellular matrix
extracellular matrix
apoptotic process
heart development
inflammatory response
SMC proliferation migration
IκB kinase/NFκB signaling
calcium,potassium: sodium antiporter activity
ListHits
4
8
12
16
pvalue
0.5
0.4
0.3
0.2
0.1
0 10 20 30
B
WT
KO
-3.0 TSS 3.0 -3.0 TSS 3.0 kb
WT
KO
-3.0 TSS 3.0
ChIP-target
4771
379
761
0
1271
0
2485
RNA-seq up
RNA-seq down
proteinaceous extracellular matrix
extracellular matrix
extracellular matrix organization
apoptotic process
regulation of apoptotic process
inflammatory response
collagen fibril organization
calcium ion binding
Notch signaling pathway
regulation of angiogenesis
ListHits
10
20
30
40
50
pvalue
0.03
0.02
0.01
2 3 4
C
WT
KO
-3.0 TSS 3.0 -3.0 TSS 3.0 kb
WT
KO
-3.0 TSS 3.0
ChIP-target
343
33
80
0
1617
0
3166
RNA-seq up
RNA-seq down
apoptotic process
negative regulation of apoptotic process
positive regulation of apoptotic signaling
proteinaceous extracellular matrix
extracellular matrix
collagen fibril organization
SMC proliferation migration
Regulation of Inflammatory
ListHits
2
4
6
8
pvalue
0.25
0.20
0.15
0.10
0.05
10 20 30 40
D
H3K9me3
H3K9ac
H3K4me3
WT
KO
Adamts4
Mmp9
E
H3K9me3
H3K9ac
H3K4me3
WT
KO
Col1a2
Nlrp3
Bcl2

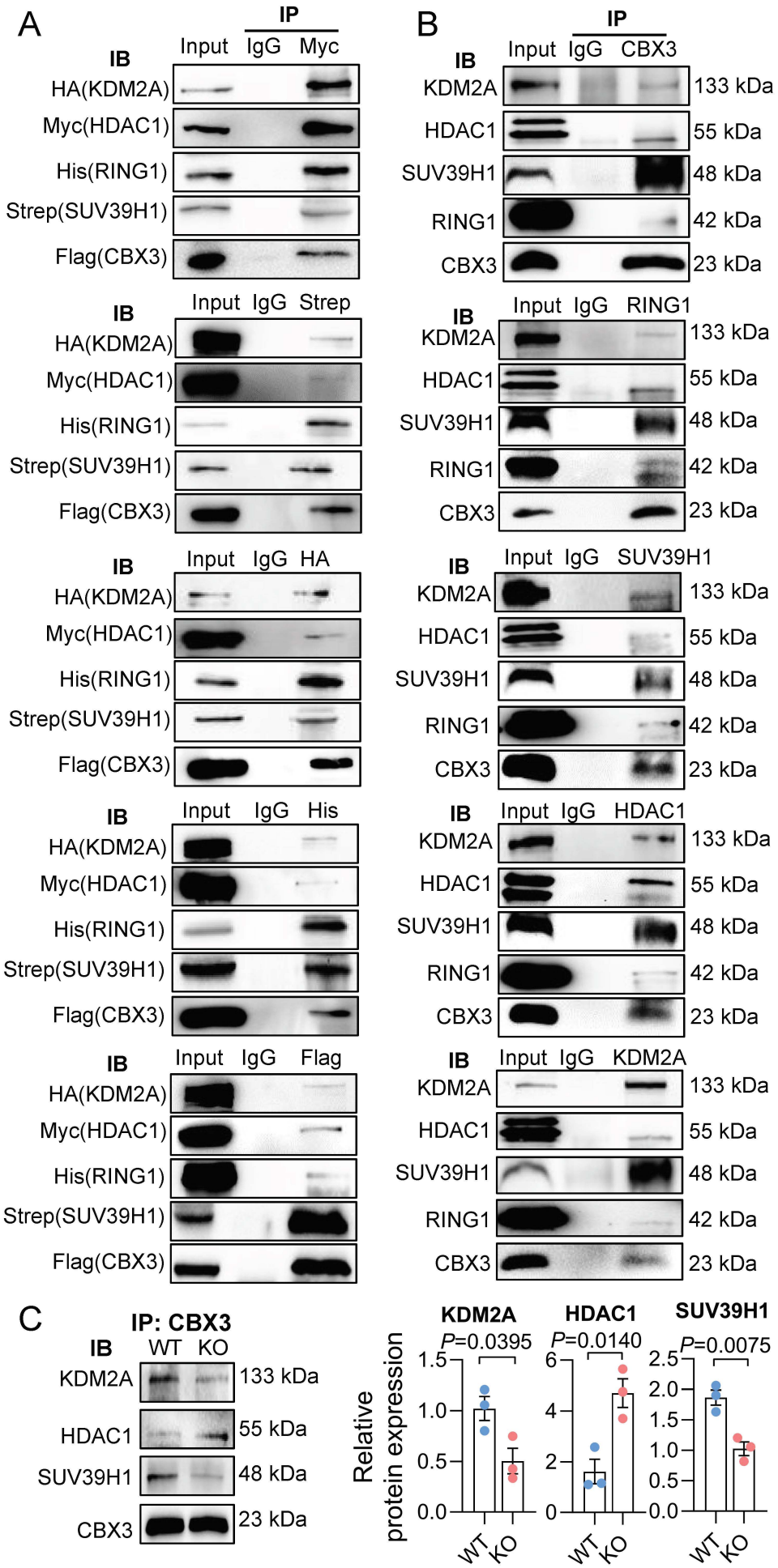
A
IP
Input IgG Myc
IB
HA(KDM2A)
Myc(HDAC1)
His(RING1)
Strep(SUV39H1)
Flag(CBX3)
Input IgG Strep
Input IgG HA
Input IgG His
Input IgG Flag
B
IP
Input IgG CBX3
Input IgG RING1
Input IgG SUV39H1
Input IgG HDAC1
Input IgG KDM2A
KDM2A
HDAC1
SUV39H1
RING1
CBX3
133 kDa
55 kDa
48 kDa
42 kDa
23 kDa
C
IP: CBX3
IB WT KO
KDM2A
HDAC1
SUV39H1
CBX3
133 kDa
55 kDa
48 kDa
23 kDa
KDM2A
HDAC1
SUV39H1
P=0.0395
P=0.0140
P=0.0075
Relative protein expression
1.5
1.0
0.5
0.0
6
4
2
0
2.5
2.0
1.5
1.0
0.5
0.0
WT
KO

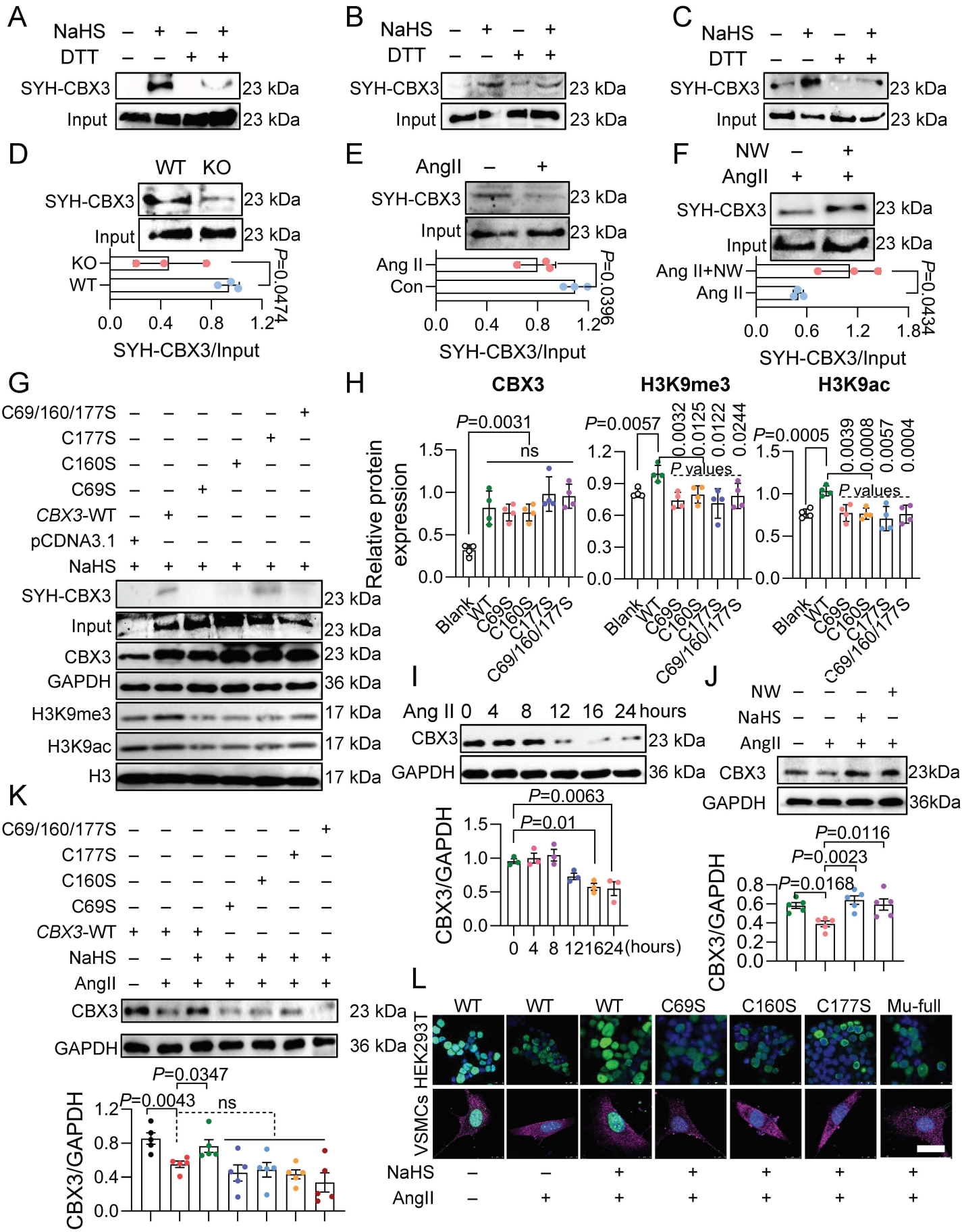
A
NaHS – + – +
DTT – – + +
SYH-CBX3
Input
23 kDa
B
C
D
WT KO
KO
WT
P=0.0474
SYH-CBX3/Input
E
AngII – +
Ang II
Con
P=0.0396
F
NW – +
AngII + +
Ang II+NW
Ang II
P=0.0434
G
C69/160/177S
C177S
C160S
C69S
CBX3-WT
pCDNA3.1
CBX3
GAPDH
H3K9me3
H3K9ac
H3
36 kDa
17 kDa
H
CBX3
H3K9me3
H3K9ac
Relative protein expression
P=0.0031
ns
P=0.0057
P values
P=0.0005
Blank
WT
C69S
C160S
C177S
C69/160/177S
I
Ang II 0 4 8 12 16 24 hours
CBX3/GAPDH
P=0.0063
P=0.01
0 4 8 12 16 24(hours)
J
NW – – – +
NaHS – – + –
AngII – + + +
23kDa
36kDa
P=0.0116
P=0.0023
P=0.0168
K
P=0.0347
P=0.0043
ns
L
WT
C69S
C160S
C177S
Mu-full
HEK293T
VSMCs
NaHS – – + + + + +
AngII – + + + + + +

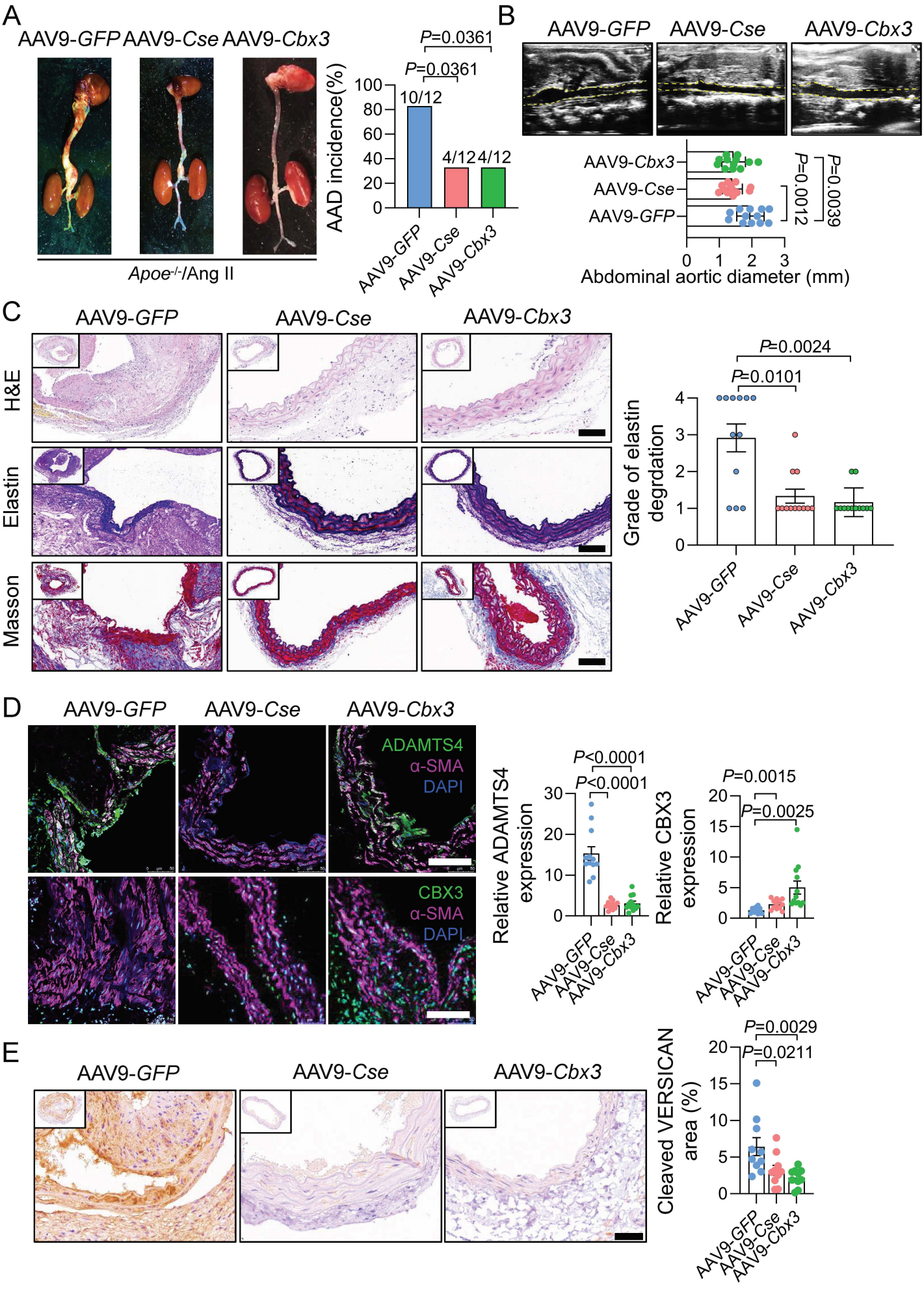
A
AAV9-GFP AAV9-Cse AAV9-Cbx3
Apoe-/-/Ang II
AAD incidence(%)
P=0.0361
P=0.0361
10/12
4/12
4/12
AAV9-GFP
AAV9-Cse
AAV9-Cbx3
B
AAV9-GFP
AAV9-Cse
AAV9-Cbx3
P=0.0039
P=0.0012
Abdominal aortic diameter (mm)
C
AAV9-GFP
AAV9-Cse
AAV9-Cbx3
H&E
Elastin
Masson
P=0.0024
P=0.0101
Grade of elastin degrdation
D
ADAMTS4
α-SMA
DAPI
CBX3
Relative ADAMTS4 expression
P<0.0001
Relative CBX3 expression
P=0.0015
P=0.0025
E
Cleaved VERSICAN area (%)
P=0.0029
P=0.0211